

Supporting Information for

**Cobalt Metal Enables Ultrahigh-Efficiency, Long-Life, and Dendrite-Free Aqueous
Multivalent Batteries**

*Songyang Chang,¹ Wentao Hou,¹ Angelica Del Valle-Perez,¹ Irfan Ullah,¹ Xiaoyu Du,¹ Lisandro Cunci,¹ Gerardo Morell,² and Xianyong Wu^{*1}*

¹S. Chang, W. Hou, A. D. Valle-Perez, I. Ullah, X. Du, L. Cunci, and X. Wu

Department of Chemistry, University of Puerto Rico-Rio Piedras Campus, San Juan, PR 00925-2537, USA

E-mail: xianyong.wu@upr.edu

²G. Morell

Department of Physics, University of Puerto Rico-Rio Piedras Campus, San Juan, PR, 00925-2537, USA

Experimental methods

1. Chemicals and materials

Cobalt chloride (purum p.a., anhydrous, purity $\geq 98.0\%$), cobalt nitrate hexahydrate (ACS reagent, purity $\geq 98.0\%$), cobalt sulfate (purity $\geq 99.0\%$), and lower-purity cobalt chloride (97% purity), potassium chloride (purity $\geq 99.0\%$), lithium chloride (purity $\geq 99\%$), and cobalt powders ($\geq 99.0\%$) were purchased from Sigma Aldrich. The LiMn_2O_4 material was purchased from MTI corporation.

2. Material synthesis

The $\text{KCuFe}(\text{CN})_6$ material was prepared using a co-precipitation method. In this process, 40 mL of 0.1 M $\text{Cu}(\text{NO}_3)_2 \cdot 3\text{H}_2\text{O}$ and 40 mL of 0.1 M $\text{K}_3\text{Fe}(\text{CN})_6$ were simultaneously added dropwise into 40 mL of water with continuous stirring. A brown precipitate formed instantly. After reacting for 4 hours, the precipitates were washed and centrifuged several times, which were allowed to dry naturally in air.

The $\text{FeFe}(\text{CN})_6$ material was prepared using a solution-based precipitation method. Specifically, 40 mL of 0.1 m $\text{K}_3\text{Fe}(\text{CN})_6$ solution was slowly added to 80 mL of 0.1 m FeCl_3 solution under magnetic stirring, and the solution was maintained at 60 °C for 6 h. After cooling to room temperature, the precipitate was obtained by centrifugation, washed several times with deionized water and ethanol, and finally dried in an oven at 60 °C.

3. Physical characterization

The XRD patterns of the cobalt, $\text{KCuFe}(\text{CN})_6$, LiMn_2O_4 , and $\text{FeFe}(\text{CN})_6$ powders were tested on the Rigaku SuperNova equipped with a HyPix3000 X-ray detector and Cu-K α radiation source ($\lambda = 1.5406 \text{ \AA}$). The SEM images and EDS mapping of the cathode materials and plated Co metals were recorded at a field emission scanning electron microscope (SEM, JEOL, JSM-6480LV).

4. Electrode preparation

To make the Co electrode, the commercial cobalt powders were first ground with Ketjen black carbon in an 8:1 mass ratio, then mixed with polytetrafluoroethylene (PTFE) binder in the 8:1:1 mass ratio, and lastly rolled into a self-standing film. The film was punched into circular shapes for use, with a diameter of 1/2 inch (1.27 cm). The Co electrode thickness is 0.66 mm, and the active mass loading is $\sim 59 \text{ mg cm}^{-2}$.

Regarding the cathode, $\text{KCuFe}(\text{CN})_6$, $\text{FeFe}(\text{CN})_6$ (or LiMn_2O_4) powders were mixed with the Ketjen black carbon and polyvinylidene difluoride (PVDF) binder in an 8:1:1 mass ratio, which

was made into a homogenous slurry with the addition of N-Methyl-2-pyrrolidone (NMP) solvent. The slurry was further coated on carbon fiber papers (AvCarb MGL370, 0.37 mm thick, 1 cm diameter) and dried in an air-forced oven at 45°C for 12 hours. The active mass loading for these cathode materials is 1.5-1.8 mg cm⁻².

5. Battery assembly and testing

The symmetrical Co|Co batteries were assembled in coin cells (2032 type), with two Co self-standing film electrodes sandwiched by two pieces of glass fiber separators. The asymmetrical Co|Cu batteries were also fabricated in coin cells, with a commercial Cu foil (9 μm thickness) working as the substrate and a Co self-standing film as the counter/reference electrode. The electrolyte is 1.0 M CoCl₂ aqueous solution (100 μL). The asymmetrical M|Cu batteries (M = Mn, Fe, Ni, and Zn) were assembled in a similar manner. The counter electrode is a self-standing Mn film, a self-standing Fe film, a Ni foil, and a Zn foil, respectively. The electrolyte is 1 M MnCl₂, 1 M FeSO₄, 1 M NiCl₂, and 1 M ZnCl₂, respectively. To test the Cu plating morphology on the Cu foil, we assembled Cu|Cu symmetrical batteries and directly plated Cu powders on the initial Cu foil substrate.

The hybrid Co|KCuFe(CN)₆, Co|FeFe(CN)₆ and Co|LiMn₂O₄ batteries were assembled in Swagelok cells with anti-corrosion titanium rod as current collectors. The electrolyte used for Co|KCuFe(CN)₆ and Co|FeFe(CN)₆ batteries is 1 M CoCl₂ + 1 M KCl, while the electrolyte for Co|LiMn₂O₄ batteries is 1 M CoCl₂ + 1 M LiCl. The electrolyte amount is 200-300 μL.

To exclude the interference of the dissolved oxygen and prevent the electrode oxidization (such as Mn, Fe, and Co), all these electrolytes used in this work were purged with nitrogen gas for 30 minutes before use. Besides, all batteries were fabricated in a portable glove box with inert gas purging.

The Galvanostatic charge/discharge tests were performed on the Landt battery tester (CT3002AU). Tafel tests, cyclic voltammetry, and electrochemical impedance spectra (EIS) were obtained on a Biologic SP-150 Potentiostat. EIS was performed over a frequency range of 0.02-100 kHz. The Tafel test was conducted at a scan rate of 5.0 mV s⁻¹. All electrochemical characterizations were conducted at room temperature (25°C).

Table S1. The comparison of transition metals in terms of the molar mass, standard electrode potential, acid dissociation constant (pK_a), gravimetric capacity, density, volumetric capacity, and price.

| Elements | Molar mass / $g\ mol^{-1}$ | Redox potentials / V vs. SHE | pK_a | Gravimetric capacity / $mAh\ g^{-1}$ | Metal density / $g\ cm^{-3}$ | Volumetric capacity / $mAh\ cm^{-3}$ | Price / USD kg^{-1} |
|----------|----------------------------|------------------------------|--------|--------------------------------------|------------------------------|--------------------------------------|-----------------------|
| Mn | 54.94 | -1.18 | 10.6 | 976 | 7.476 | 7297 | 1.82 |
| Fe | 55.85 | -0.44 | 9.4 | 960 | 7.874 | 7559 | 0.424 |
| Ni | 58.69 | -0.26 | 9.9 | 913 | 8.907 | 8132 | 13.9 |
| Cu | 63.55 | +0.34 | 7.5 | 844 | 8.935 | 7541 | 6.00 |
| Zn | 65.38 | -0.76 | 9.0 | 820 | 7.140 | 5855 | 2.55 |
| Cd | 112.41 | -0.40 | 10.1 | 477 | 8.650 | 4126 | 2.73 |
| In | 114.82 | -0.34 | 3.9 | 700 | 7.310 | 5117 | 167 |
| Sn | 118.71 | -0.13 | 3.4 | 451 | 7.280 | 3283 | 18.7 |
| Sb | 121.76 | +0.2 | N/A | 660 | 6.680 | 4409 | 5.79 |
| Co | 58.93 | -0.28 | 9.7 | 910 | 8.834 | 8039 | 32.8 |

The acid dissociation constants of relevant M^{2+} ions are available from the analytical chemistry book (D. C. Harris, *Quantitative chemical analysis*, Macmillan, 2010.),¹ whereas the price information of these elements is obtained from Wikipedia (Price of chemical elements; https://en.wikipedia.org/wiki/Prices_of_chemical_elements).²

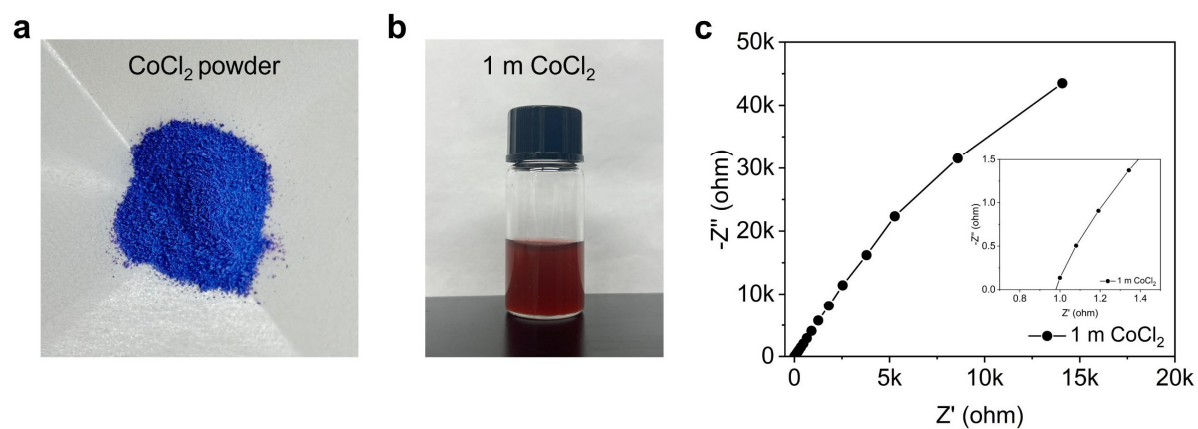


Figure S1. (a) The digital photo of the CoCl₂ powders; (b) The digital photo of the 1 M CoCl₂ solution; (c) The electrochemical impedance spectra (EIS) result of the 1 M CoCl₂ electrolyte, where two titanium rods were used as current collectors.

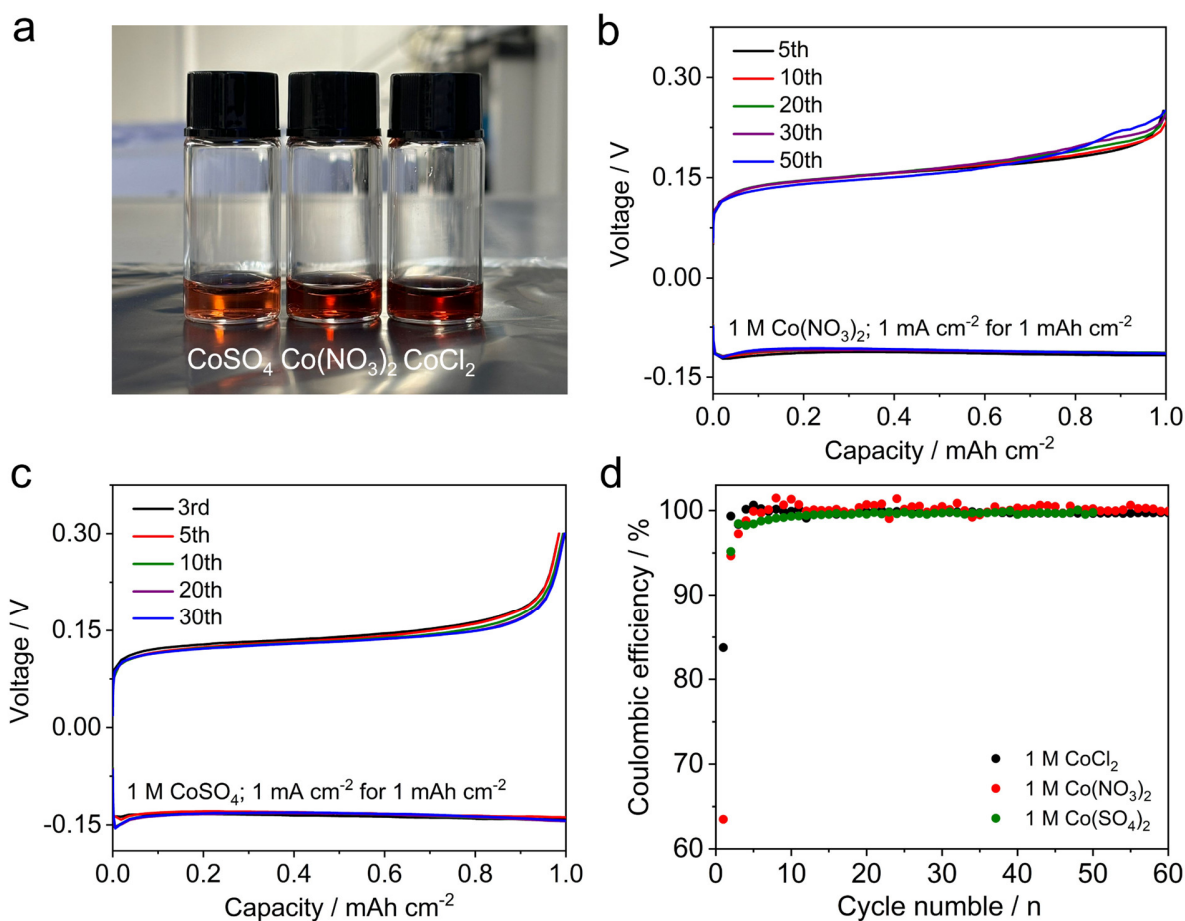


Figure S2. (a) Digital photos of 1 M Co^{2+} ion electrolytes; (b) GCD curves of the Co||Cu battery in the 1 M $\text{Co}(\text{NO}_3)_2$ electrolyte; (c) GCD curves of the Co||Cu battery in the 1 M CoSO_4 electrolyte; (d) The efficiency comparison of different electrolytes during cycling. The testing condition is 1.0 mA cm^{-2} for 1.0 mAh cm^{-2} . As shown, these three salts demonstrated similar performance for the Co metal plating, suggesting that the inherent Co^{2+}/Co redox chemistry dominated the plating process.

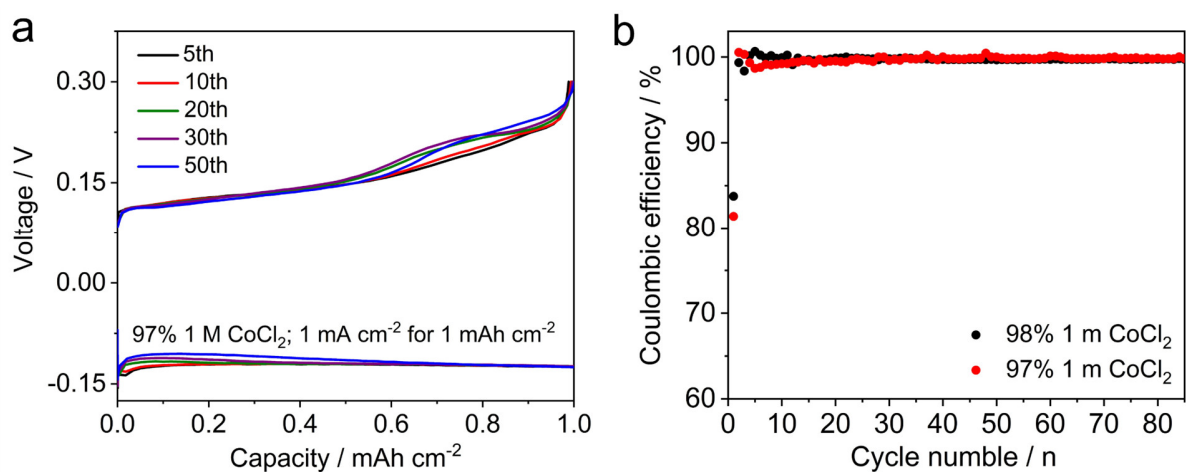


Figure S3. The Co plating performance in the low-purity CoCl₂ electrolyte (salt purity: 97%). (a) GCD curves of the asymmetrical Co/Cu battery; (b) The cycling performance comparison in the CoCl₂ electrolytes with different salt purity. As shown, these two electrolytes achieved comparable Coulombic efficiency and cycling stability, suggesting that the salt purity played a minor role in affecting the Co plating chemistry.

Table S2. The price comparison of Co powders and foils. The price was obtained from Sigma Aldrich on Feb 5, 2025.

| | Product No. | Purity | Price | USD per gram |
|------------|-------------|--------|--|--------------|
| Co powders | 1.12211 | 99+% | 138.6 \$ for 100 g | 1.39 |
| Co foils | 356867 | 99.95% | 0.1 mm, 315.9 \$ for 2.2 g | 143 |
| | | | 0.1 mm, 714 \$ for 8.8 g | 81 |
| | GF40808516 | 99.9% | Size: 10 x 10 cm, thickness: 0.25 mm, 1270 \$ each | ~57 |

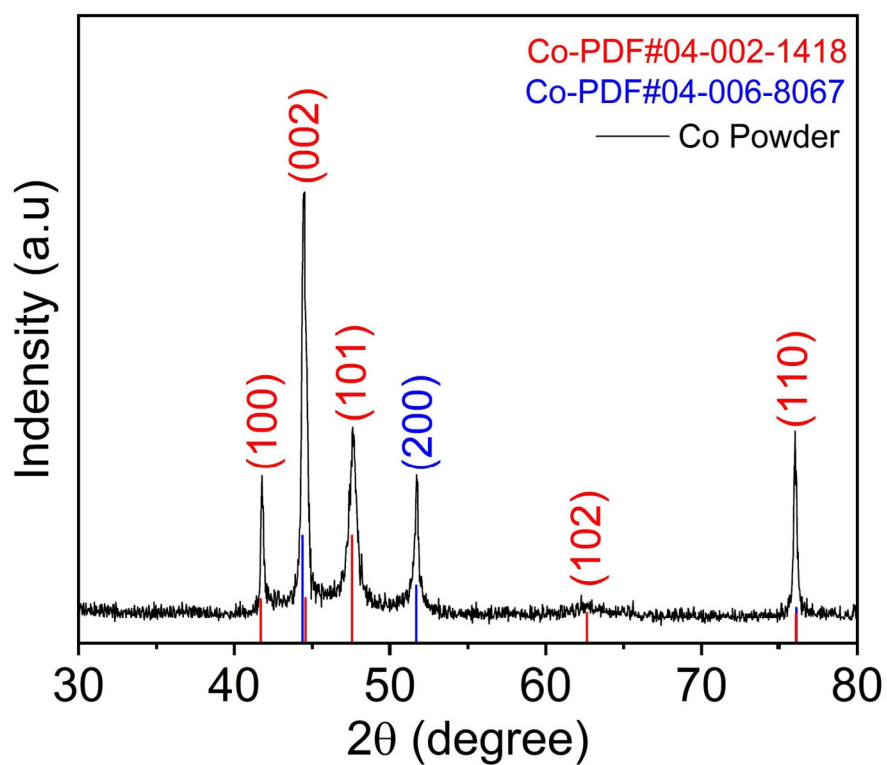


Figure S4. The XRD pattern of the pristine Co powders. Although the commercial Co powders have two different phases, all these XRD peaks are well indexed to the standard Co cards (JCPDS 02-1418; JCPDS 06-8067), which indicate high chemical purity.

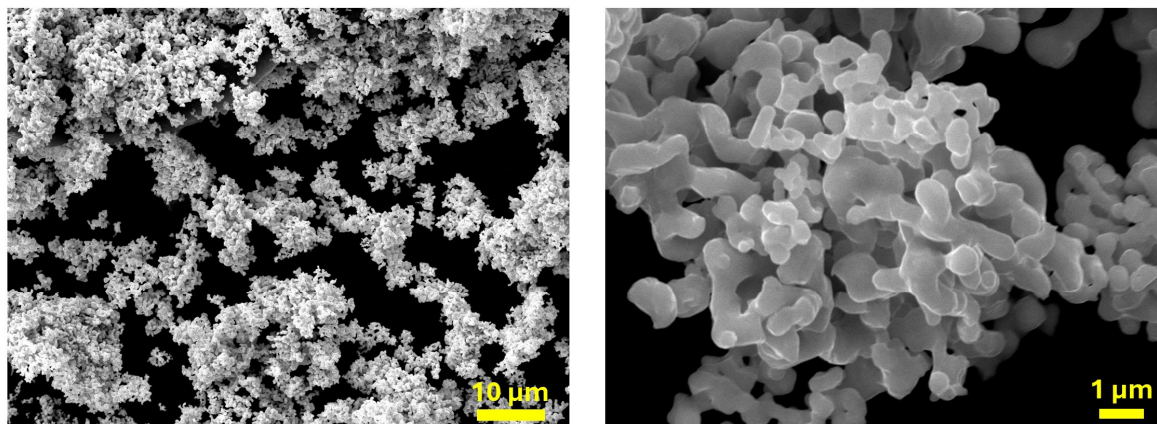


Figure S5. SEM images of the pristine Co powders. As shown, the Co powders have a quasi-spherical morphology with a particle size of 300-600 nm.

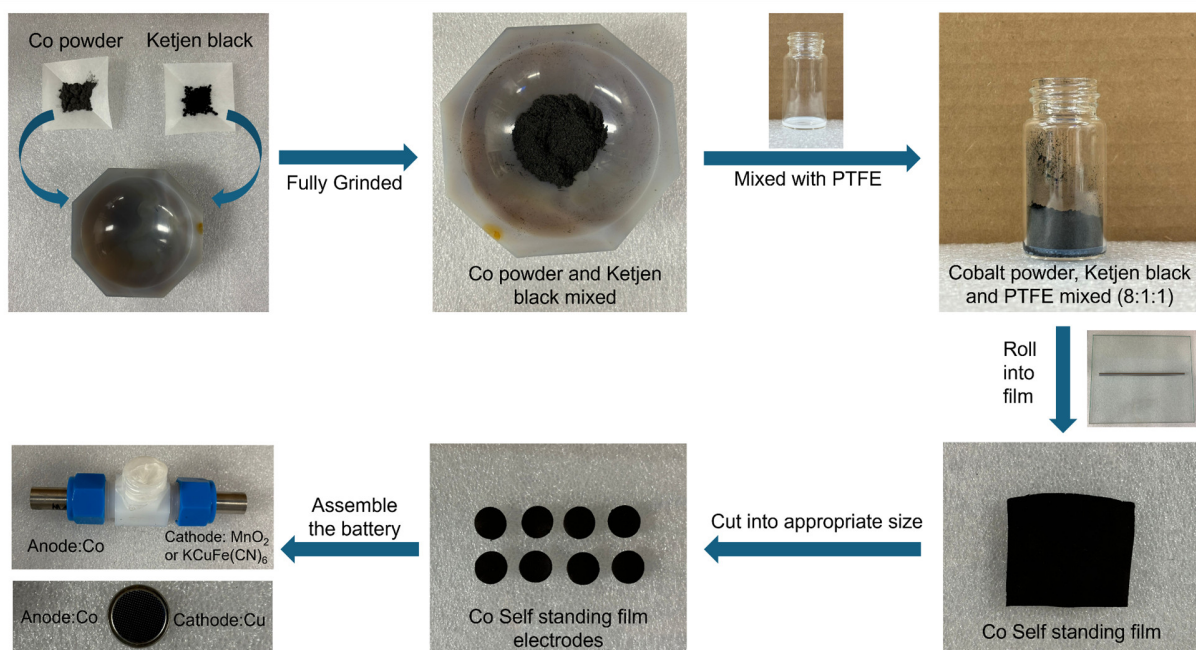


Figure S6. The preparation process of the Co self-standing films and their use in aqueous Co metal batteries.

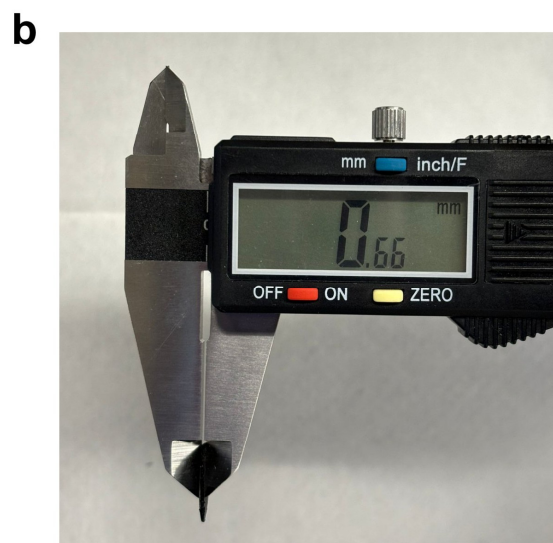
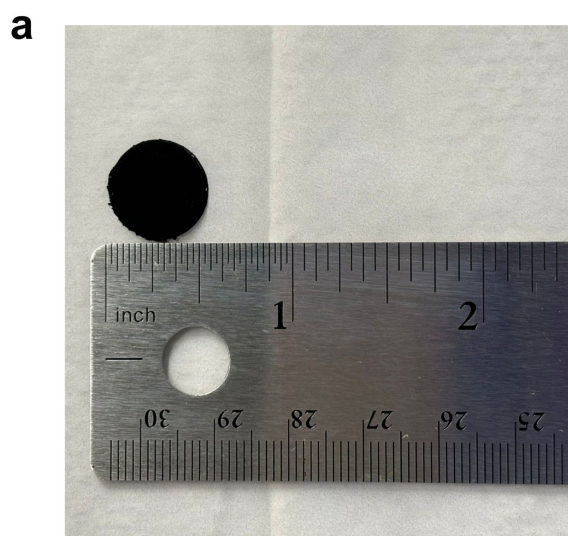


Figure S7. Digital photos of the self-standing Co electrode film. (a) The size of the film; (b) The thickness of the film. As shown, the Co self-standing film is 1.27 cm in diameter and 0.66 mm in thickness.

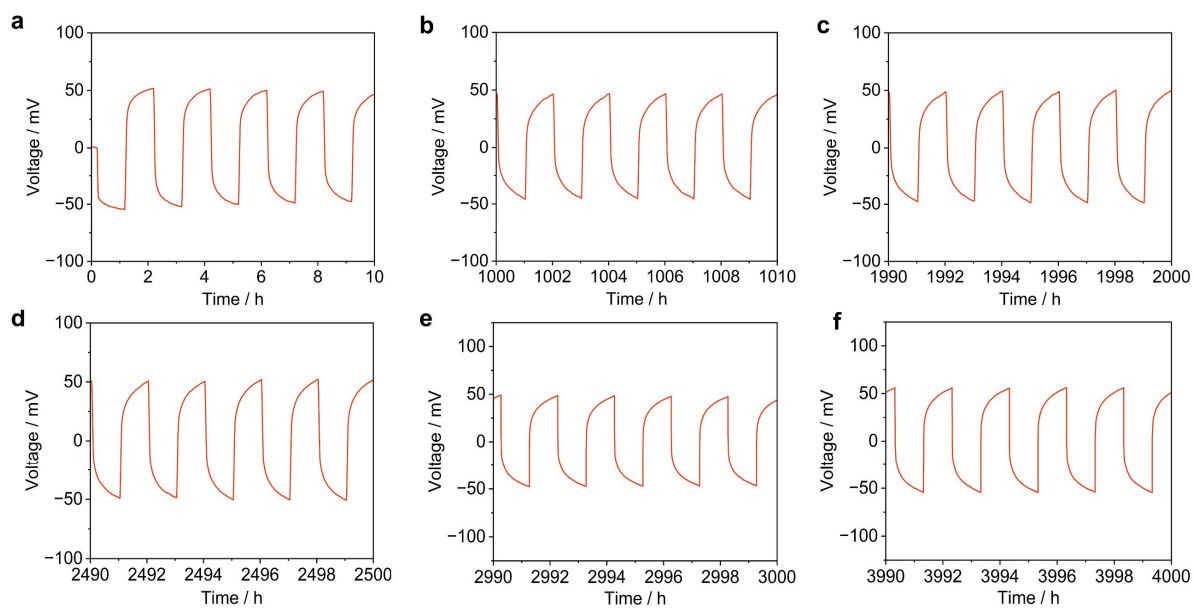


Figure S8. (a) The overall GCD curves of the ColCo symmetrical cells; (b-f) The selected GCD curves during cycling. The current density is 0.5 mA cm^{-2} , and the capacity is 0.5 mAh cm^{-2} . Each cycle has 60 minutes of charging and 60 minutes of discharging.

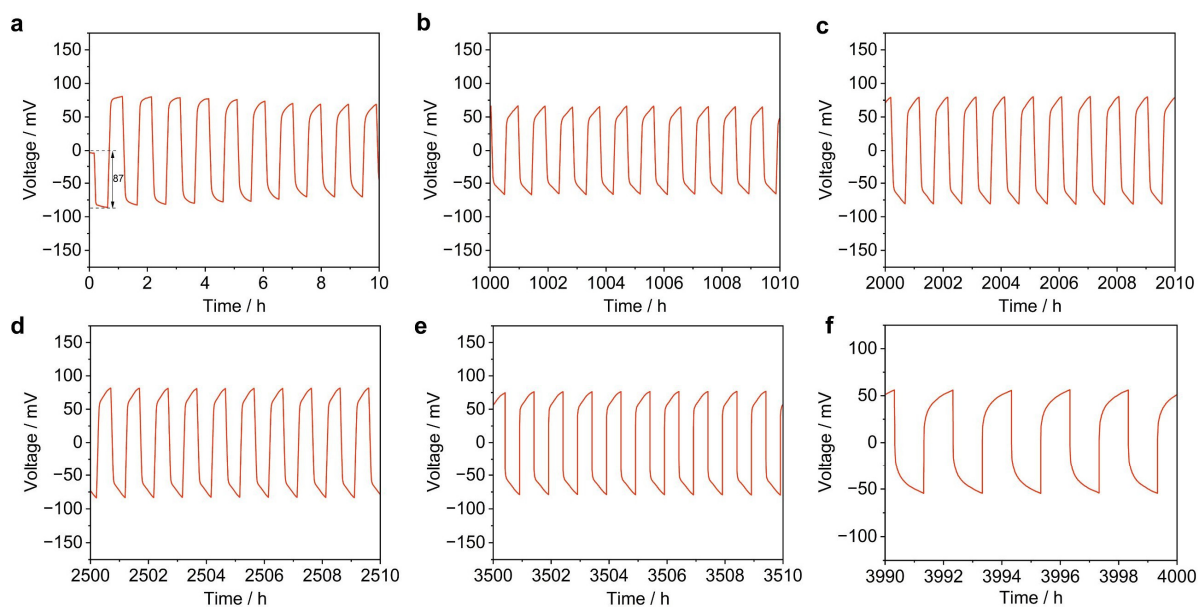


Figure S9. (a) The overall GCD curves of the Co||Co symmetrical cells; (b-d) The selected GCD curves during cycling. The current density is 1.0 mA cm^{-2} , and the capacity is 0.5 mAh cm^{-2} . Each cycle has 30 minutes of charging and 30 minutes of discharging.

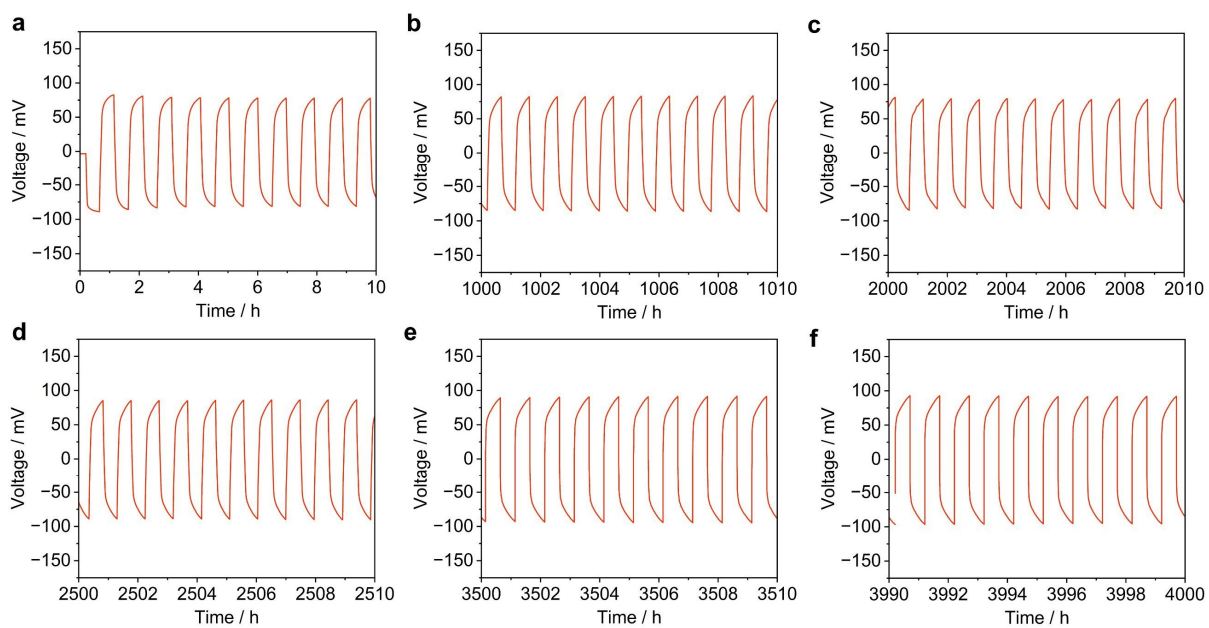


Figure S10. (a) The overall GCD curves of the Co||Co symmetrical cells; (b-d) The selected GCD curves during cycling. The current density is 2.0 mA cm^{-2} , and the capacity is 0.5 mAh cm^{-2} . Each cycle has 15 minutes of charging and 15 minutes of discharging.

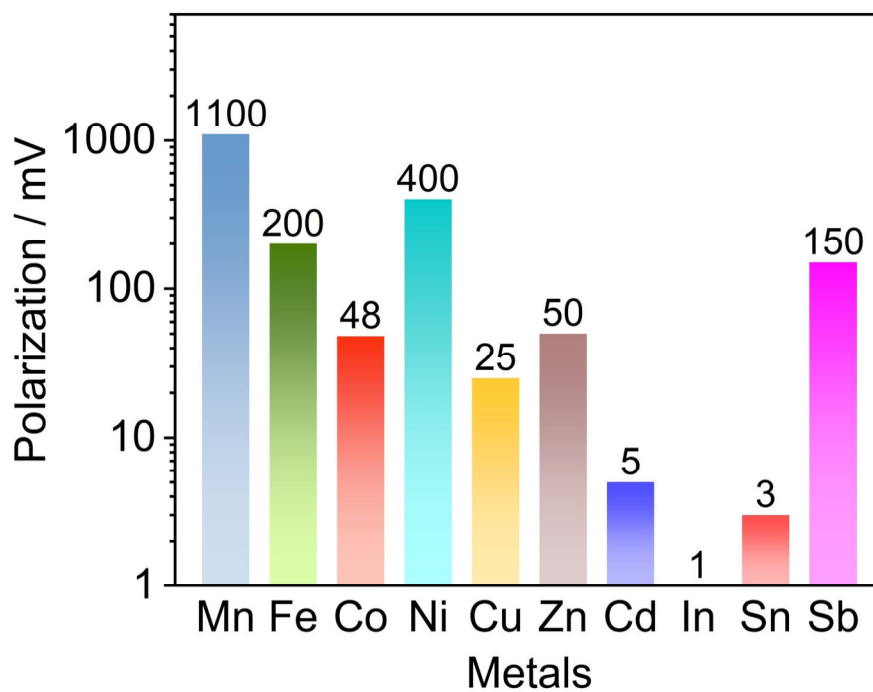


Figure S11. The polarization comparison of different metal electrodes tested under similar conditions.

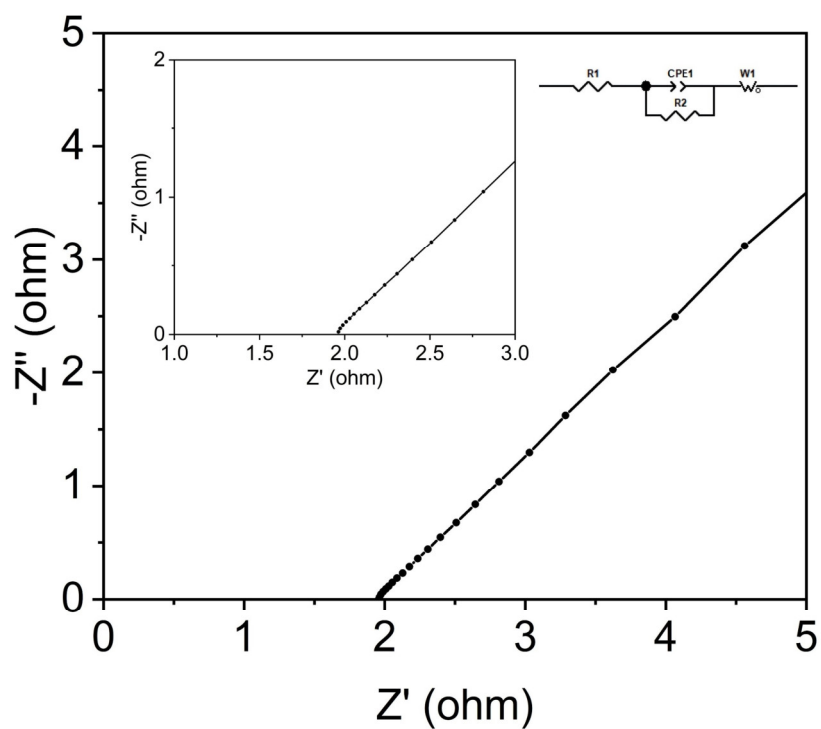


Figure S12. The EIS result of the symmetrical Co||Co battery at room temperature. The equivalent circuit diagram is provided in the figure inset. As fitted, the charge-transfer resistance (R_{CT}) is as low as ~ 0.28 ohm, suggesting fast Co^{2+}/Co reaction kinetics.

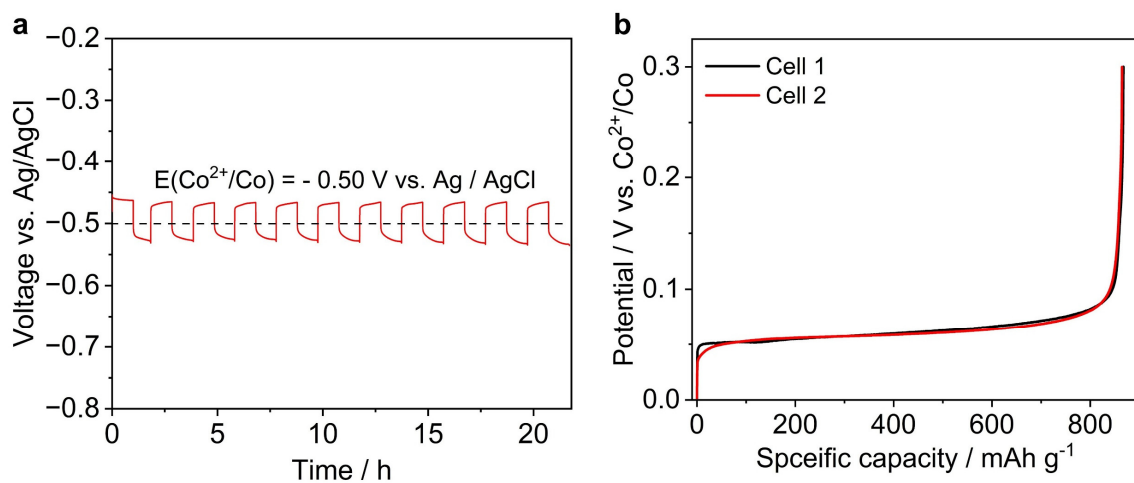


Figure S14. The reaction potential and specific capacity of the Co electrode. (a) GCD curves of the Co||Cu batteries with an Ag/AgCl reference electrode; (b) The stripping capacity of the Co electrode in the Co||Co symmetrical battery configuration (current density: 100 mAh g^{-1}). As shown, the practical Co electrode potential is $-0.5 \text{ V vs. Ag/AgCl}$, corresponding to -0.30 V vs. SHE . This potential is very close to that of the standard Co^{2+}/Co redox couple (-0.28 V vs. SHE). Besides, the Co self-standing electrode demonstrated a practical capacity of $\sim 850 \text{ mAh g}^{-1}$, close to its 2-electron theoretical capacity (910 mAh g^{-1}). These results indicate the two-electron Co^{2+}/Co redox reaction without other Co valance states.

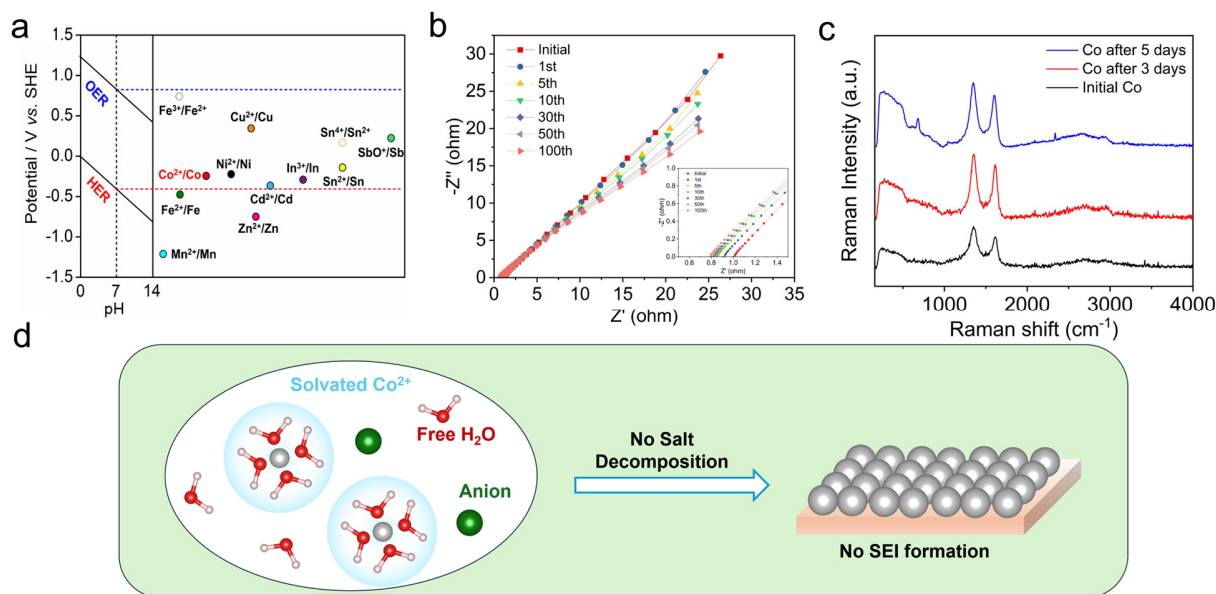


Figure S15. (a) The Pourbaix diagram of water and the standard M^{n+}/M electrode potentials; (b) EIS results of the symmetrical Co||Co battery after different cycling numbers (1 mA cm^{-2} for 0.5 mAh cm^{-2}); (c) Raman results of Co self-standing film electrode before and after cycling at 1 mA cm^{-2} for 0.5 mAh cm^{-2} ; (d) Reaction mechanism of aqueous Co metal batteries.

The standard Co^{2+}/Co couple resides well in the water stability window (**Figure S15a**), which fundamentally avoids the HER side reaction. In practice, the Co^{2+}/Co potential is experimentally determined as -0.30 V vs. SHE (**Figure S14**), and the HER potential at $\text{pH} = 5.8$ is calculated as $-0.059\text{pH} = -0.34 \text{ V}$. Therefore, the practical Co^{2+}/Co potential is still higher than HER, suggesting that no (or minimal) water decomposition side reaction will take place. As a result, the Co electrode demonstrates a constant charge-transfer resistance during cycling (**Figure S15b**), implying the absence of surface passivation layer. Raman analysis is a surface-sensitive technique that can detect surface passivation or generation of new compounds. As shown in **Figure S15c**, the Raman spectra of the cycled Co electrodes are nearly identical to that of the initial Co electrode, further supporting the absence of the passivation layer. In conclusion, the Co metal exhibits a highly reversible plating reaction in aqueous electrolytes without causing significant HER or electrode passivation (**Figure S15d**), thus explaining the long calendar life (4000 hours), constant polarization ($\sim 50 \text{ mV}$), and ultrahigh efficiency ($\sim 99.9\%$) in the main context.

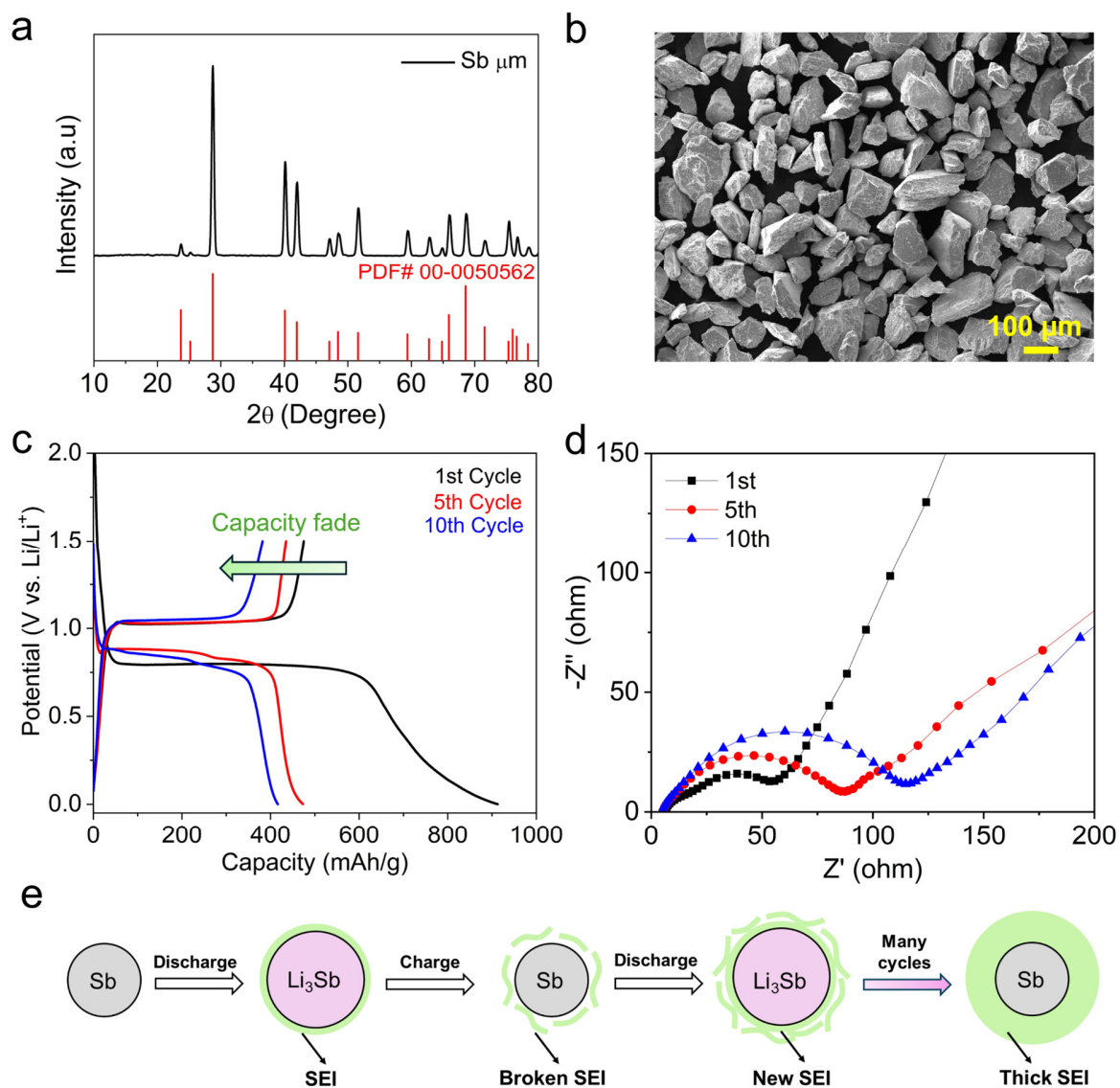


Figure S16. The characterization of Sb alloy materials and batteries. (a) XRD pattern of Sb; (b) SEM image of Sb; (c) GCD curve of Li||Sb batteries in 1 M LiPF₆/EC-DMC at 50 mA g⁻¹; (d) The EIS response of Li||Sb batteries; (e) The scheme of the SEI breakage and reformation in Li||Sb batteries.

Solid-electrolyte interphase (SEI) formation is a common phenomenon in conventional Li-ion batteries (LIBs), which is usually a result of salt and solvent decomposition during the discharge process. The SEI is an ion-conductor but electron-insulator, whose composition is

generally a solid-state mixture of both inorganic and organic compounds, such as LiF, Li₂O, Li₂CO₃, organic (dilithium ethylene glycol dicarbonate (Li₂EDC), and lithium alkyl carbonates, *etc.*

To facilitate the readers' understanding between LIBs and aqueous batteries, we also utilized antimony (Sb), a typical alloy material, to demonstrate how SEI evolves during cycling and its impact on the battery performance. As shown, the Sb material is phase pure and exhibits a micro-sized particle morphology (**Figure S16a-b**). In the LiPF₆/EC-DMC electrolyte, the Li||Sb battery discharge to 0 V vs. Li⁺/Li, which will trigger the electrolyte decomposition and the formation of SEI. However, the Li||Sb battery suffers from a continuous capacity fading (**Figure S16c**), due to its significant volume change. We utilize electrochemical impedance spectroscopy (EIS) to gain insights into the SEI evolution, because the semi-circle is a good indicator of the charge-transfer resistance (R_{ct}) on the Sb electrode surface. As shown, there is a progressive increment in the EIS semi-circle (**Figure S16d**), indicating continuous SEI layer growth and thickening. This accounts for the capacity fading. We also plot a scheme to delineate the SEI formation and thickening process (**Figure S16e**): during discharge, the SEI forms on the Li₃Sb surface. However, the large volume change during charge will damage the initial SEI. In another round of discharge, there will be new SEI formation, which, again, is subject to the following SEI damage. Overall, the SEI layer is in a dynamic breakage/reformation process and grows with cycling, leading to the increasing battery resistance and capacity fading.

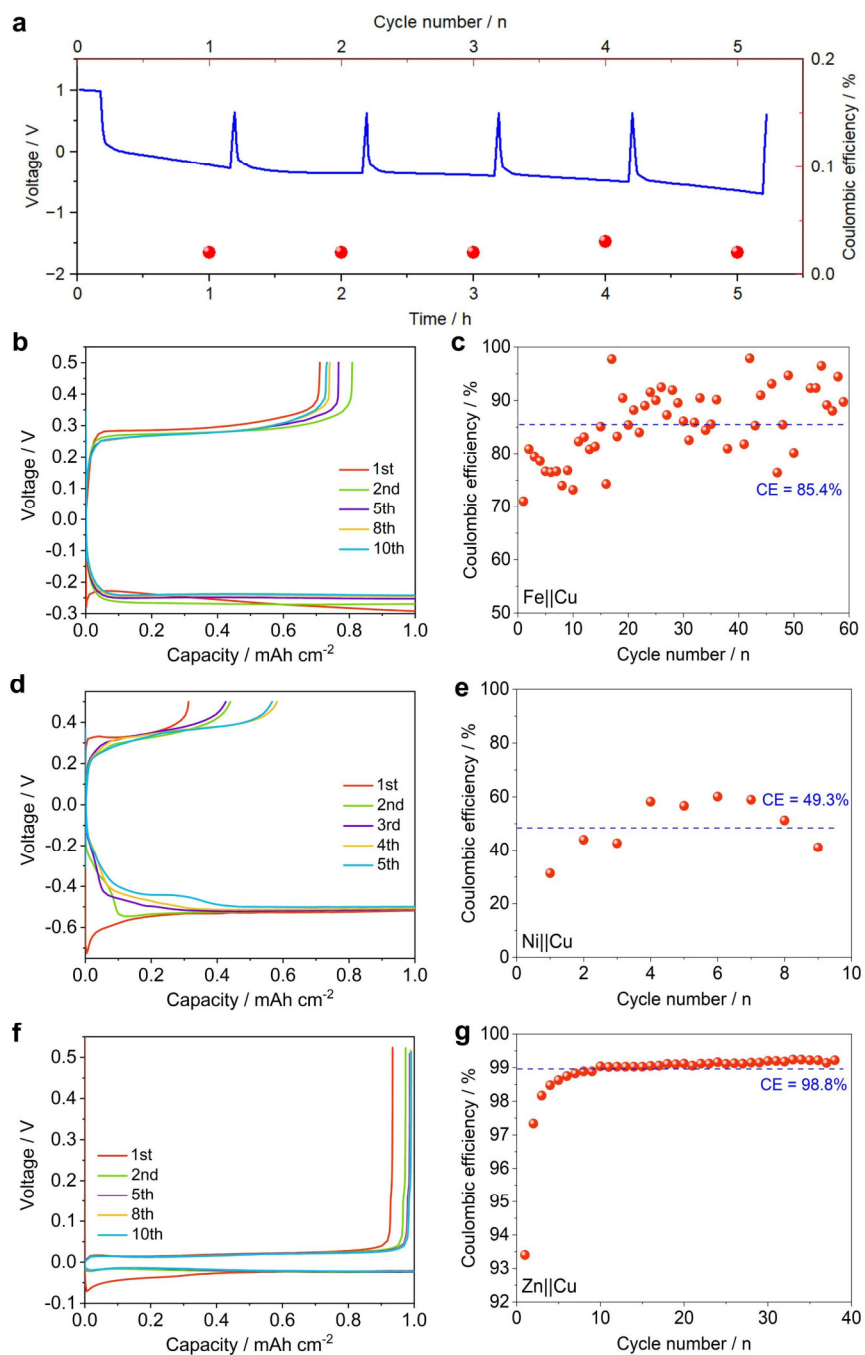


Figure S17. Selected GCD curves and Coulombic efficiencies of different transition metals in the asymmetric M||Cu battery configuration (M = Mn, Fe, Ni, and Zn). (a) Mn||Cu batteries; (b-c) Fe||Cu batteries; (d-e) Ni||Cu batteries; (f-g) Zn||Cu batteries. The testing condition is akin to the Co||Cu batteries, namely 1.0 mA cm^{-2} for 1.0 mAh cm^{-2} . The electrolyte is 1 M MnCl_2 , 1 M FeSO_4 , 1 M NiCl_2 , and 1 M ZnCl_2 , respectively.

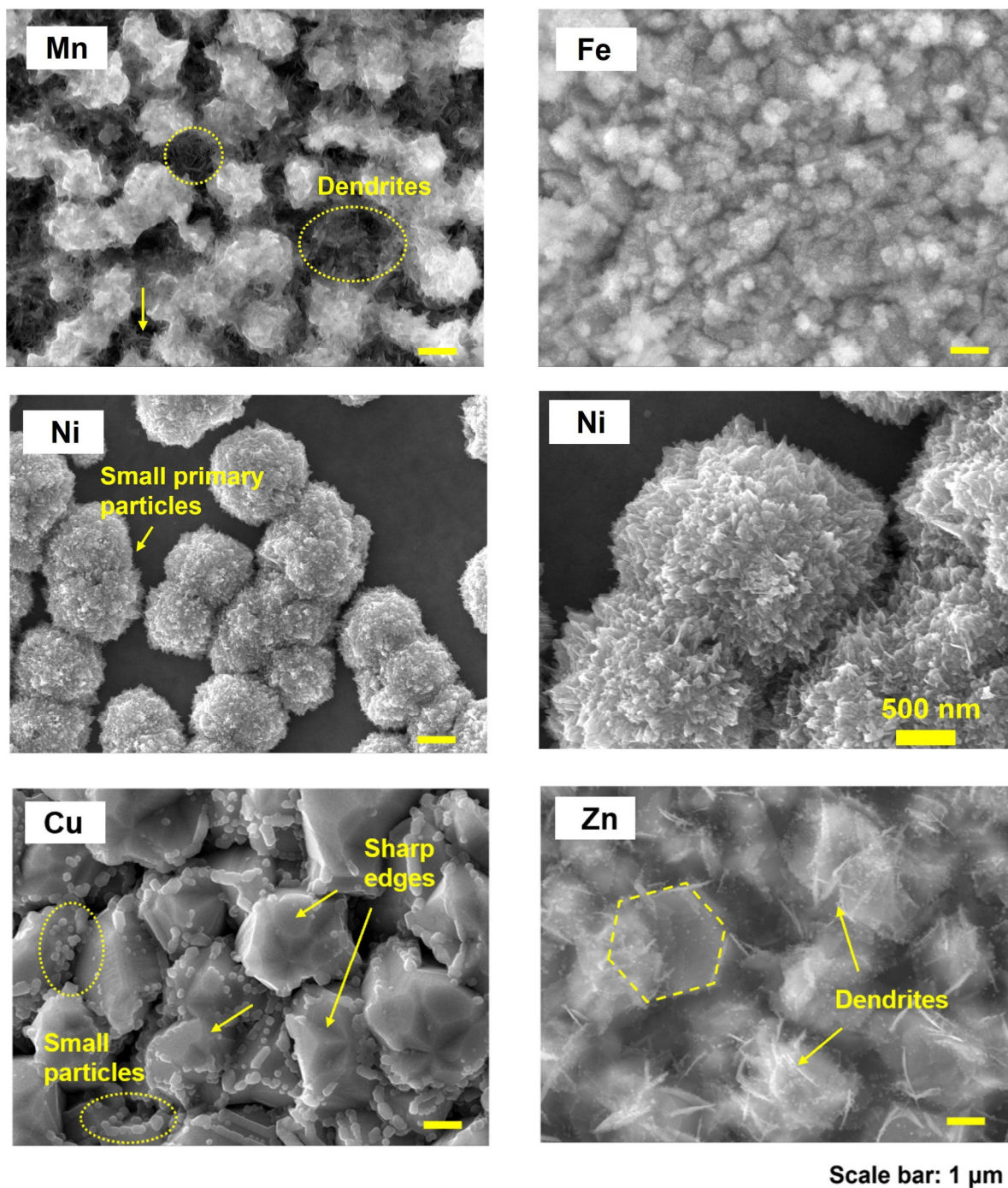


Figure S18. The plating morphology of transition metals on the Cu foil substrate in their corresponding 1 M electrolyte. The testing condition is 1.0 mA cm^{-2} current for 1.0 mAh cm^{-2} capacity.

As shown in **Figure S18**, the plated Mn metal appears as irregularly aggregated clusters, and some plate-like dendrites are evident among these clusters.

Although Fe and Ni metals exhibit a spherical morphology, their particle sizes are much smaller than the Co metal. Specifically, the primary particle size of Fe is in the range of 100-200 nm, whereas the primary particle size of Ni is even smaller, being 50-100 nm. This will significantly increase their contact area with the electrolyte, causing more side reactions to happen.

Cu metal shows an irregular polyhedral chunk-type morphology with relatively sharp edges. Besides, there are some small particles surrounding these chunks. The wide size distribution range indicates a less uniform plating process.

Zn metal exhibits some tendency to form hexagonal particles, as marked in the dashed yellow color. However, many dendritic and protruding plates are evident, which can easily pierce the separator and cause short circuits.

In comparison, the Co metal demonstrates a uniform, micro-sized, densely packed, and spherically aggregated morphology, which can effectively minimize the surface area and boost the plating efficiency.

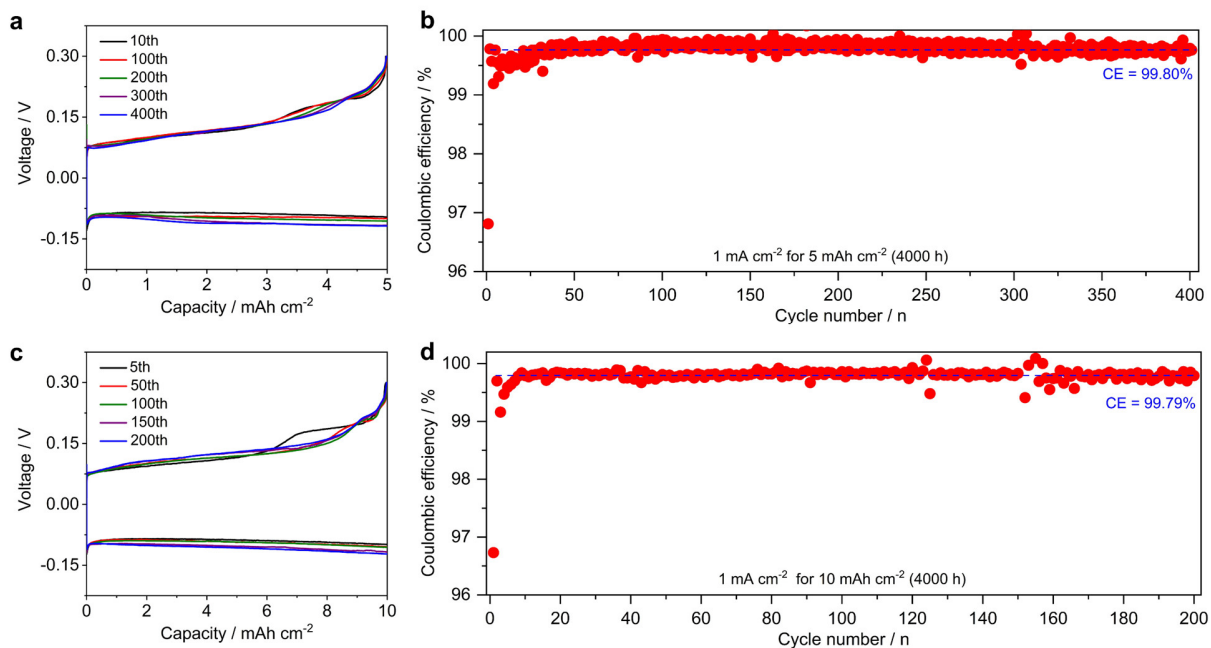


Figure S19. (a-b) The GCD curves and cycling performance of Co||Cu batteries at 1 mA cm⁻² current and 5 mAh cm⁻² capacity; (c-d) The GCD curves and cycling performance of Co||Cu batteries at 1 mA cm⁻² current and 10 mAh cm⁻² capacity.

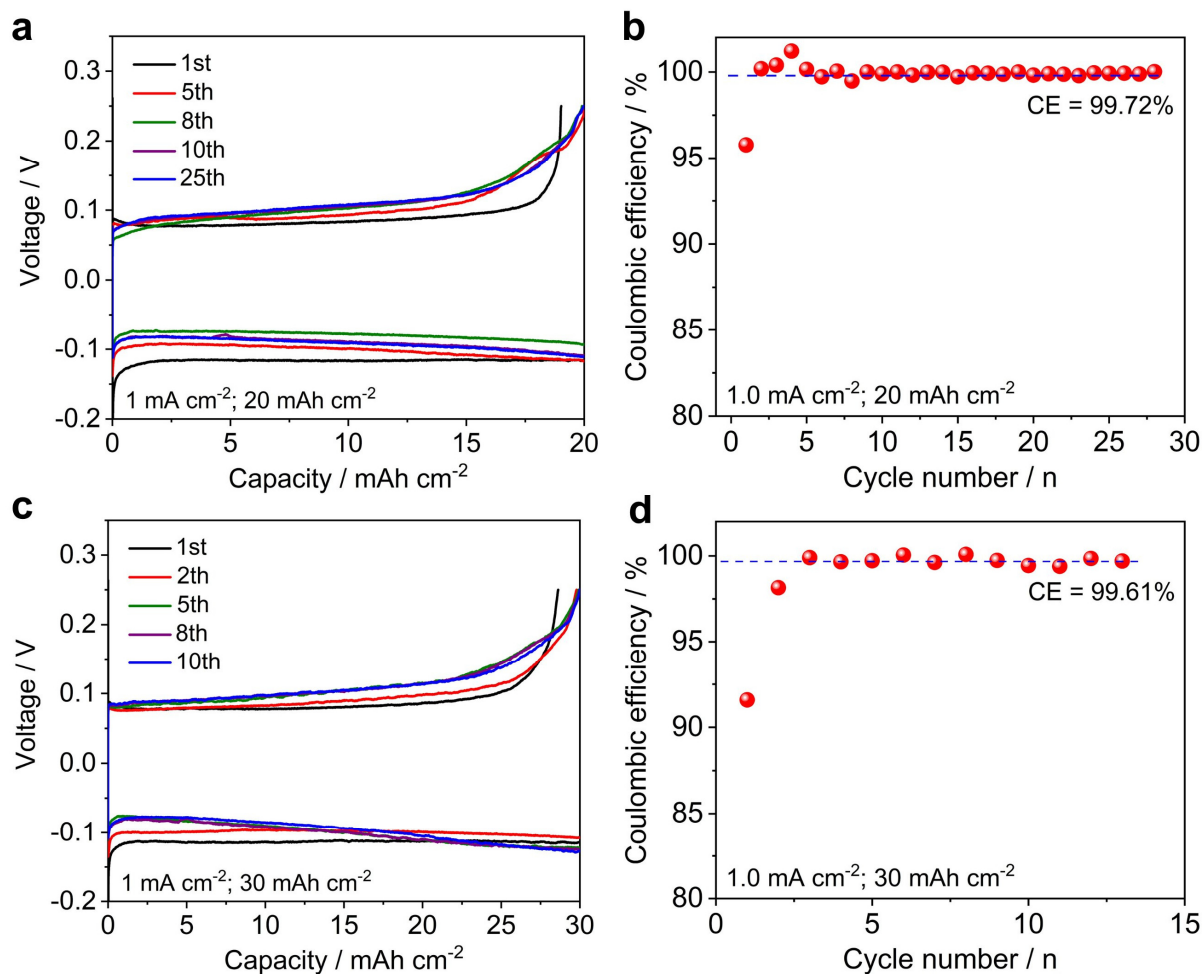


Figure S20. (a-b) The GCD curves and cycling performance of Co||Cu batteries at 1 mA cm⁻² current and 20 mAh cm⁻² capacity; (c-d) The GCD curves and cycling performance of Co||Cu batteries at 1 mA cm⁻² current and 30 mAh cm⁻² capacity.

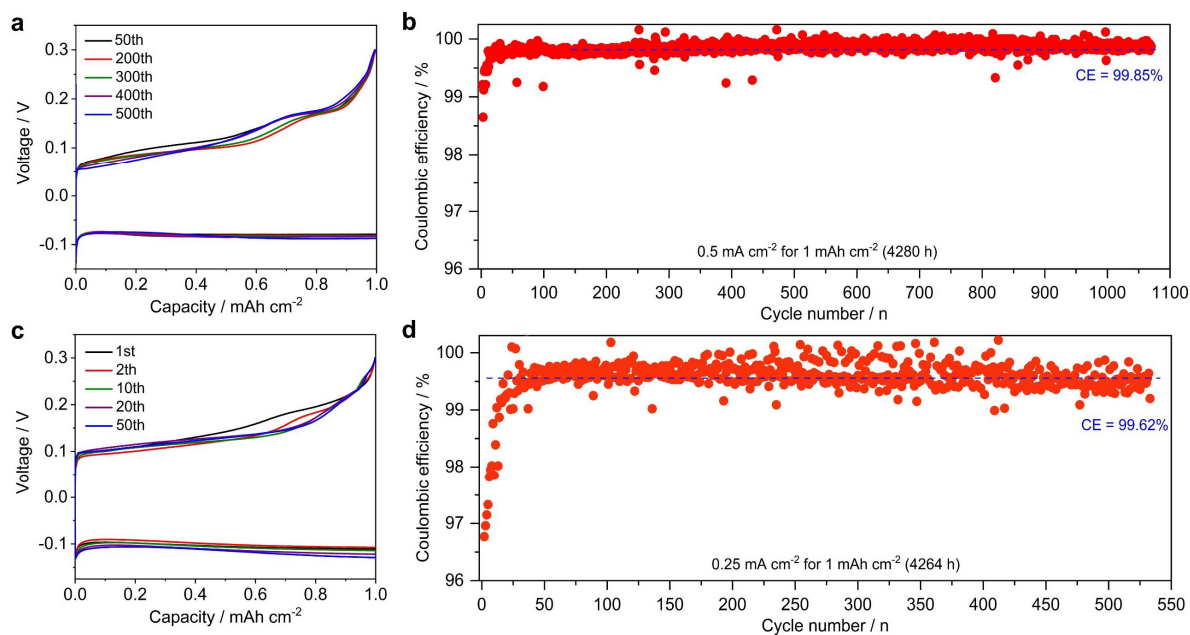


Figure S21. (a-b) The GCD curves and cycling performance of Co||Cu batteries at 0.5 mA cm⁻² current and 1 mAh cm⁻² capacity; (c-d) The GCD curves and cycling performance of Co||Cu batteries at 0.25 mA cm⁻² current and 1 mAh cm⁻² capacity.

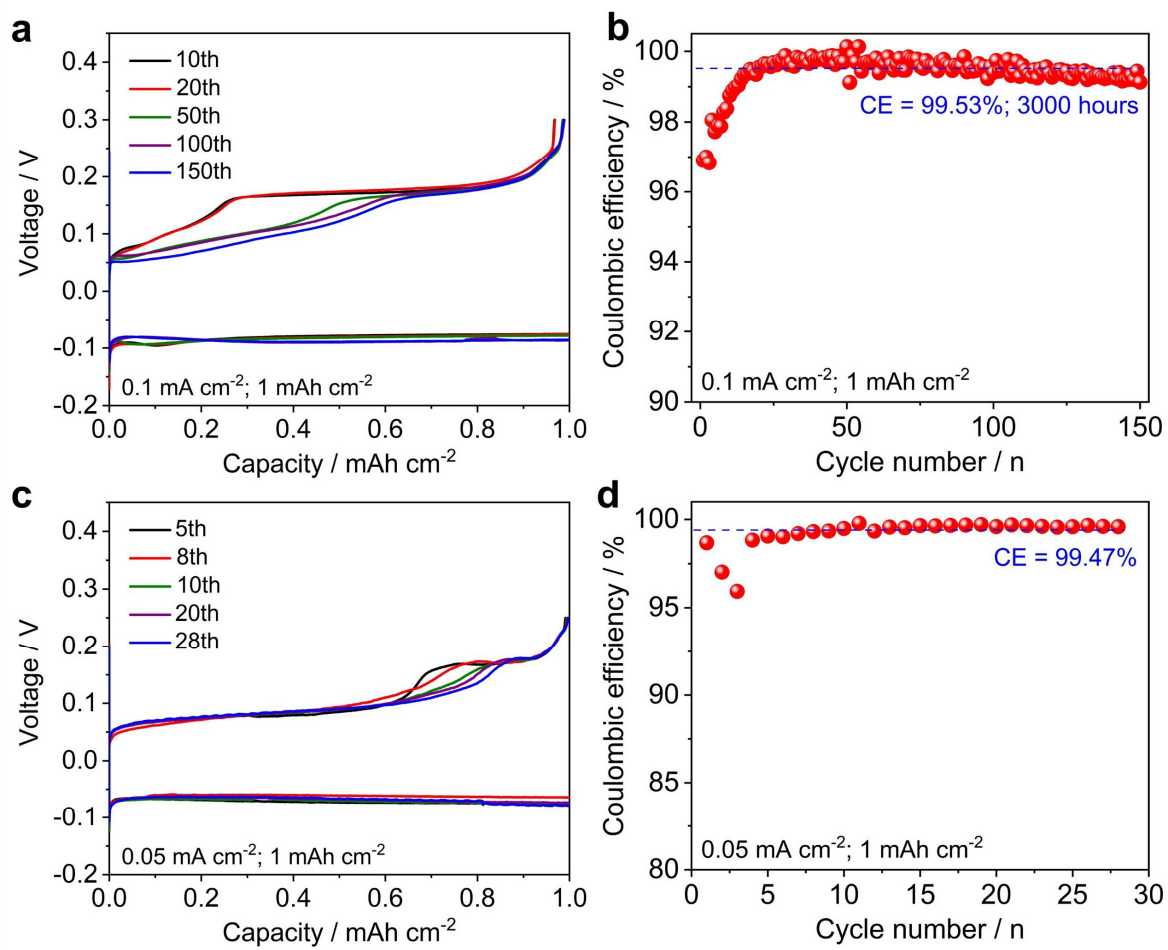


Figure S22. (a-b) The GCD curves and cycling performance of Co||Cu batteries at 0.1 mA cm^{-2} current and 1 mAh cm^{-2} capacity; (c-d) The GCD curves and cycling performance of Co||Cu batteries at 0.05 mA cm^{-2} current and 1 mAh cm^{-2} capacity.

Table S3. The performance comparison between our Co metal anode and some representative transition metal batteries.

| Anodes | Electrolytes | Plating Current (mA cm ⁻²) | Capacity (mAh cm ⁻²) | CE% | Calander Life / hours | Ref |
|--------|---|--|----------------------------------|--------|-----------------------|-----------|
| Mn | SeO ₂ -additive MnSO ₄ | 180 | -- | 73 | -- | [3] |
| Fe | FeSO ₄ | 0.125 | 0.5 | 90.7 | 400 | [4] |
| | 5+1 M FeCl ₂ /ZnI ₂ | 0.5 | 0.5 | 98 | 2500 | [5] |
| | 0.5 M FeCl ₂ + 4.5 M MgCl ₂ | 1 | 1 | 99.1 | 200 | [6] |
| Ni | 21mLiTFSI + 1mNi(OTf) ₂ | 0.1 | 0.1 | 99.5 | 1400 | [7] |
| | 1m NiCl ₂ | 50 | 0.5 | 99.05 | 300 | [8] |
| Cu | CuSO ₄ | 1 | 0.5 | 99.4 | 500 | [9] |
| Sn | 1 M SnCl ₂ | 1 | 1 | 99.97% | 3000 | [10] |
| Cd | 1 M CdCl ₂ | 1 | 1 | 99.92% | 3243 | [11] |
| In | 1 M InCl ₃ | 1 | 1 | 99.8% | 5360 | [12] |
| Zn | 4 m Zn(OTF) ₂ + 0.5 m Me ₃ EtNOT + H ₂ O | 0.5 | 0.5 | 99.8 | 2000 | [13] |
| | DICH | 2 | 1 | 99.7 | 1000 | [14] |
| | 1M Zn(DFTFSI) ₂ | 1 | 4 | 99.6 | 1600 | [15] |
| | WSE | 1 | 1 | 99.9 | 600 | [16] |
| | DHFIP ₄ | 0.5 | 1 | 99.9 | 2600 | [17] |
| Co | 1 m CoCl ₂ | 1 | 1 | 99.86 | 4200 | This work |
| | | 1 | 5 | 99.80 | 4000 | |
| | | 1 | 10 | 99.79 | 4000 | |
| | | 1 | 20 | 99.72 | 1120 | |
| | | 1 | 30 | 99.61 | 780 | |
| | | 0.5 | 1 | 99.85 | 4280 | |
| | | 0.25 | 1 | 99.62 | 4264 | |
| | | 0.1 | 1 | 99.53 | 3000 | |
| 0.05 | 1 | 99.47 | 1120 | | | |



Figure S23. (a) Digital photos of the aqueous Co metal coin cells; (b) The temperature and humidity information during the cell testing.

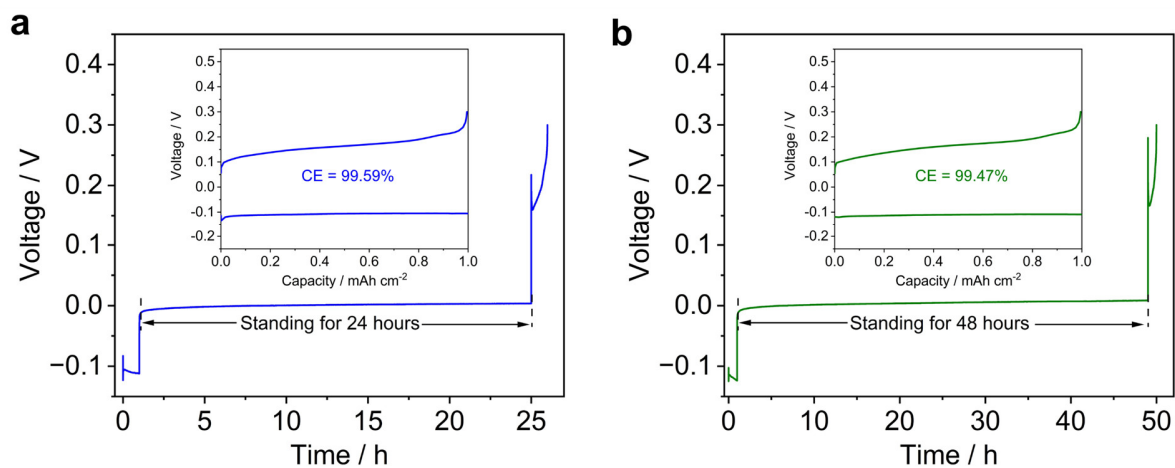


Figure S24. The plating/stripping performance of the Co electrode after different periods' resting. (a) After resting for 24 hours; (b) After resting for 48 hours. The plating current is 1 mA cm^{-2} , and the capacity is 1 mAh cm^{-2} .

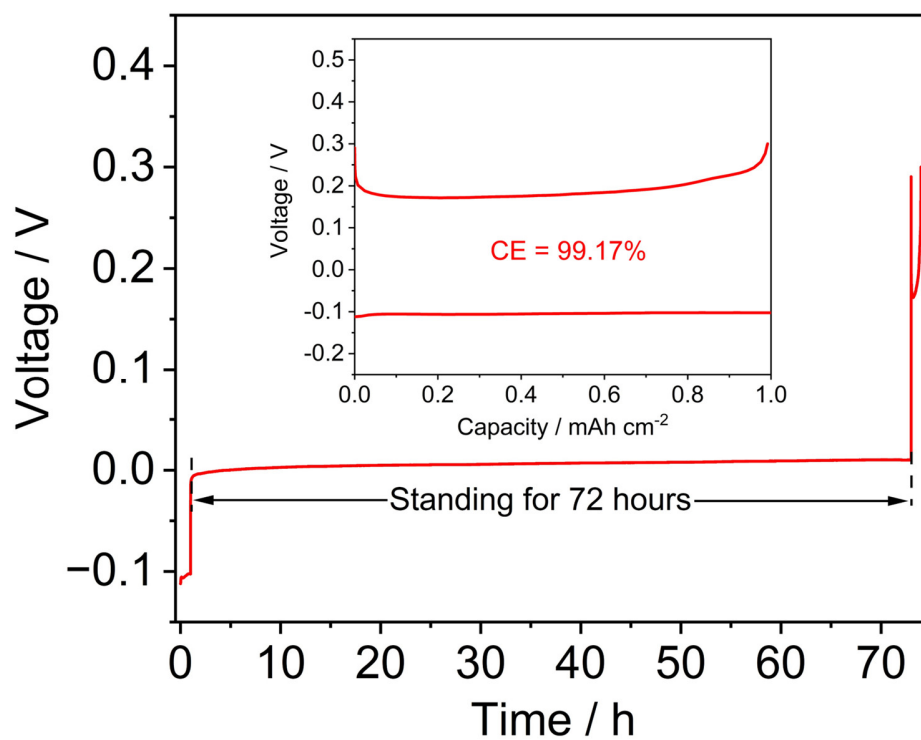


Figure S25. The plating/stripping performance of the Co electrode after 72 hours' resting. The plating current is 1 mA cm⁻², and the capacity is 1 mAh cm⁻².

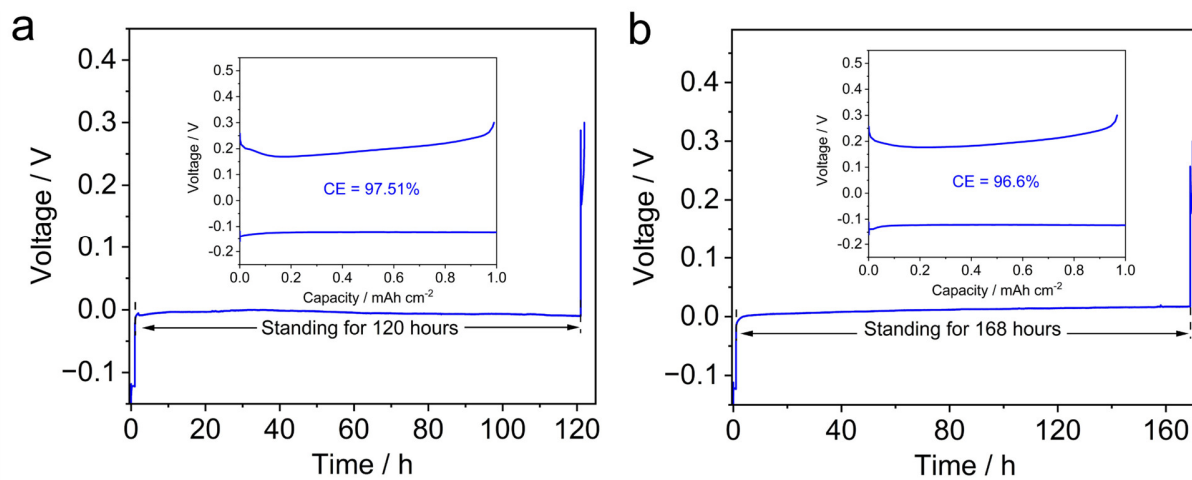


Figure S26. The plating/stripping performance of the Co electrode after different periods' resting. (a) After resting for 5 days; (b) After resting for 7 days. The plating current is 1 mA cm^{-2} , and the capacity is 1 mAh cm^{-2} .

Table S4. The self-discharge performance comparison between the Co and Zn metal.

| Battery system | Storage time | Electrolytes | CE | Reference |
|----------------|--------------|---|--------|-----------|
| Zn Cu | 0 | 1 M Zn(DFTFSI) ₂ | 99.6% | [18] |
| Zn Cu | 0 | 30 m ZnCl ₂ +10 m TMACl+5 m LiCl | 99.6% | [19] |
| Zn Cu | 0 | 20 m LiTFSI + 1 m Zn(TFSI) ₂ | 99.7% | [20] |
| Zn Cu | 0 | Molten ZnCl ₂ hydrate | 98.7% | [21] |
| Zn Cu | 0 | 30 m ZnCl ₂ + 5 m LiCl | 99.7% | [22] |
| Zn Cu | 0 | 0.5 M Zn(OTF) ₂ in trimethyl phosphate | 99.57% | [23] |
| Zn Cu | 0 | 1 M Zn(OTF) ₂ in H ₂ O/PC | 99.73% | [24] |
| Zn Cu | 0 | 2 M ZnSO ₄ +0.0085 M La(NO ₃) ₃ | 99.9% | [25] |
| Zn Cu | 0 | ZnCl ₂ in EG with molar ratio 1:4 | 99.7% | [26] |
| Zn Cu | 0 | 4 m Zn(BF ₄) ₂ /EG | 99.4% | [27] |
| Zn Cu | 24 hours | 3 m ZnSO ₄ | 97.8% | [28] |
| Zn Cu | 24 hours | 2 M ZnSO ₄ | 60% | [29] |
| Zn Ti | 24 hours | 2 M ZnSO ₄ | 74.4% | [30] |
| Co Cu | 24 hours | 1 M CoCl ₂ | 99.59% | This work |
| Co Cu | 48 hours | | 99.47% | |
| Co Cu | 72 hours | | 99.17% | |
| Co Cu | 120 hours | | 97.5% | |
| Co Cu | 168 hours | | 96.6% | |

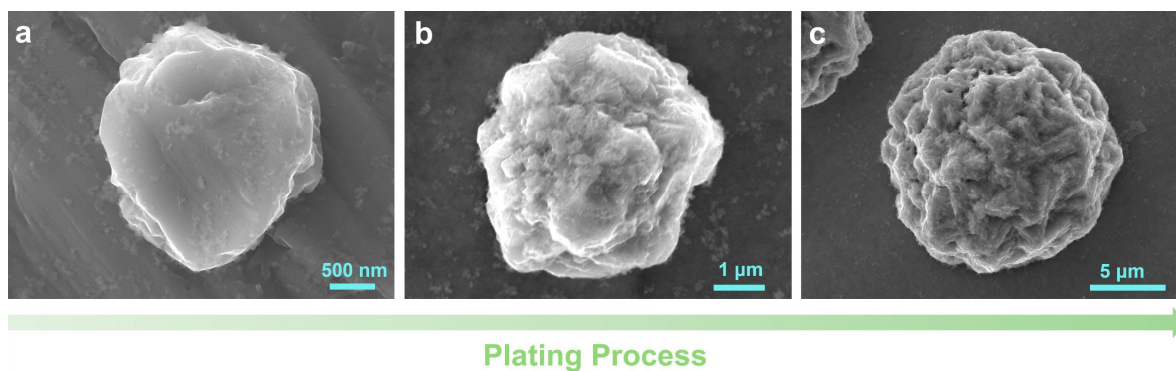


Figure S27. SEM images of the plated Co metals with higher magnification (smaller scale bar). (a) Plating for 0.2 mAh cm^{-2} ; (b) Plating for 0.5 mAh cm^{-2} ; (c) Plating for 1.0 mAh cm^{-2} . The plating current is 1.0 mA cm^{-2} .

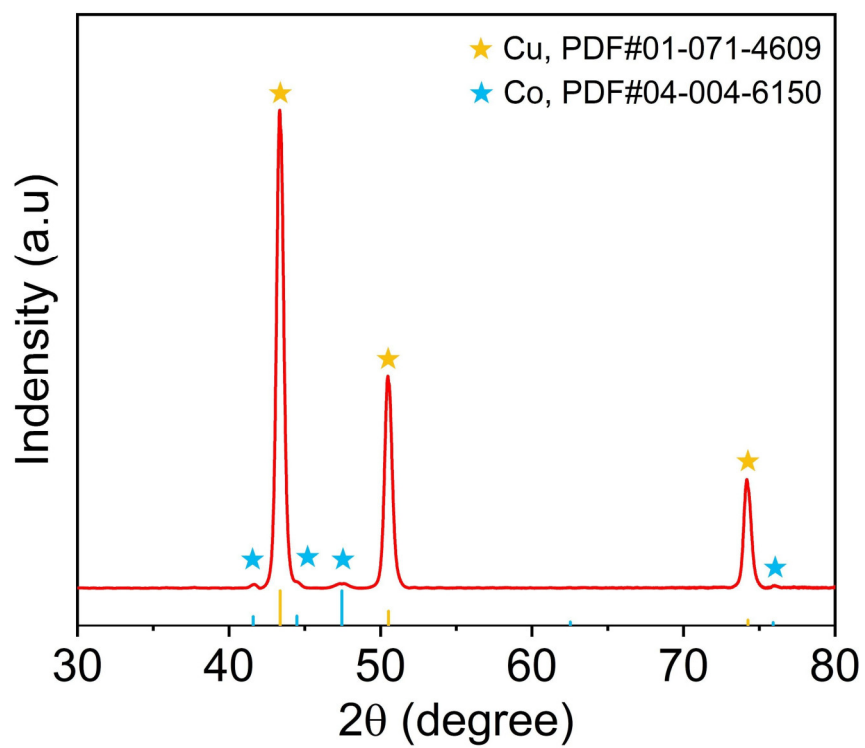


Figure S28. The XRD pattern of the plated Co metal on the Cu foil at 1.0 mA cm^{-2} current and 1.0 mAh cm^{-2} capacity.

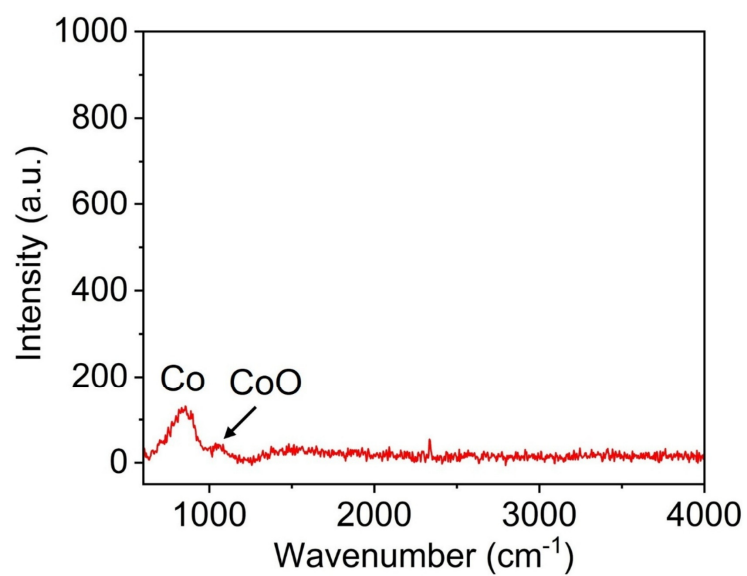


Figure S29. The Raman analysis of the deposited Co metal on the Cu foil. As shown, the Co surface does not contain noticeable electrolyte decomposition compounds, suggesting the absence of solid-electrolyte interphase (SEI). There is a minor peak attributed to the CoO, possibly due to the electrode oxidization in air.

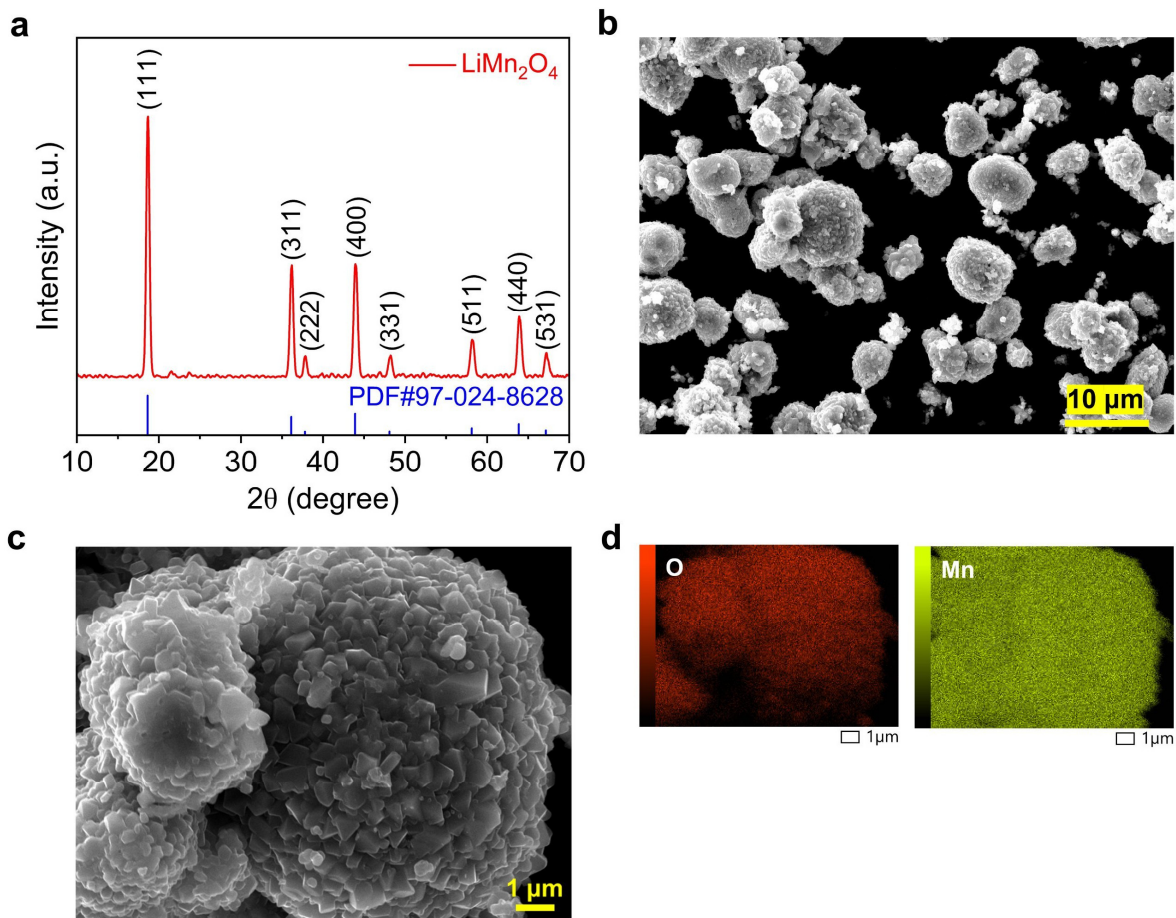
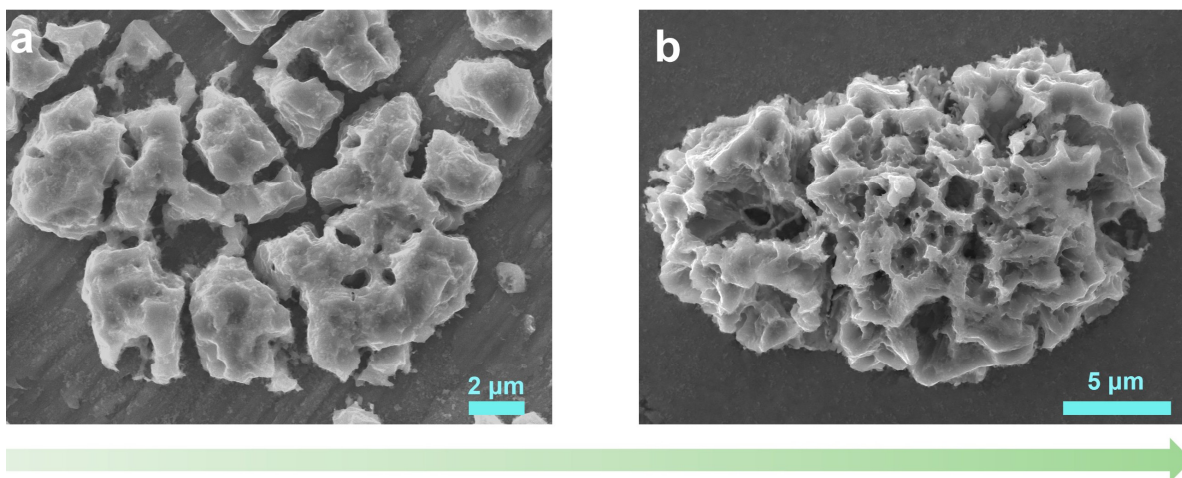


Figure S30. Physical characterizations of the commercial LiMn_2O_4 cathode. (a) The XRD pattern; (b-c) The SEM images; (d) EDS mapping results.



Stripping Process

Figure S31. SEM images of the Co metal at different stripping capacities. (a) At 0.5 mAh cm^{-2} ; (b) At 0.8 mAh cm^{-2} . The stripping current is 1.0 mA cm^{-2} . As shown, with the proceeding of the charging process, the Co metals lose more internal connections and become highly porous, indicating a gradual Co metal oxidization and dissolution.

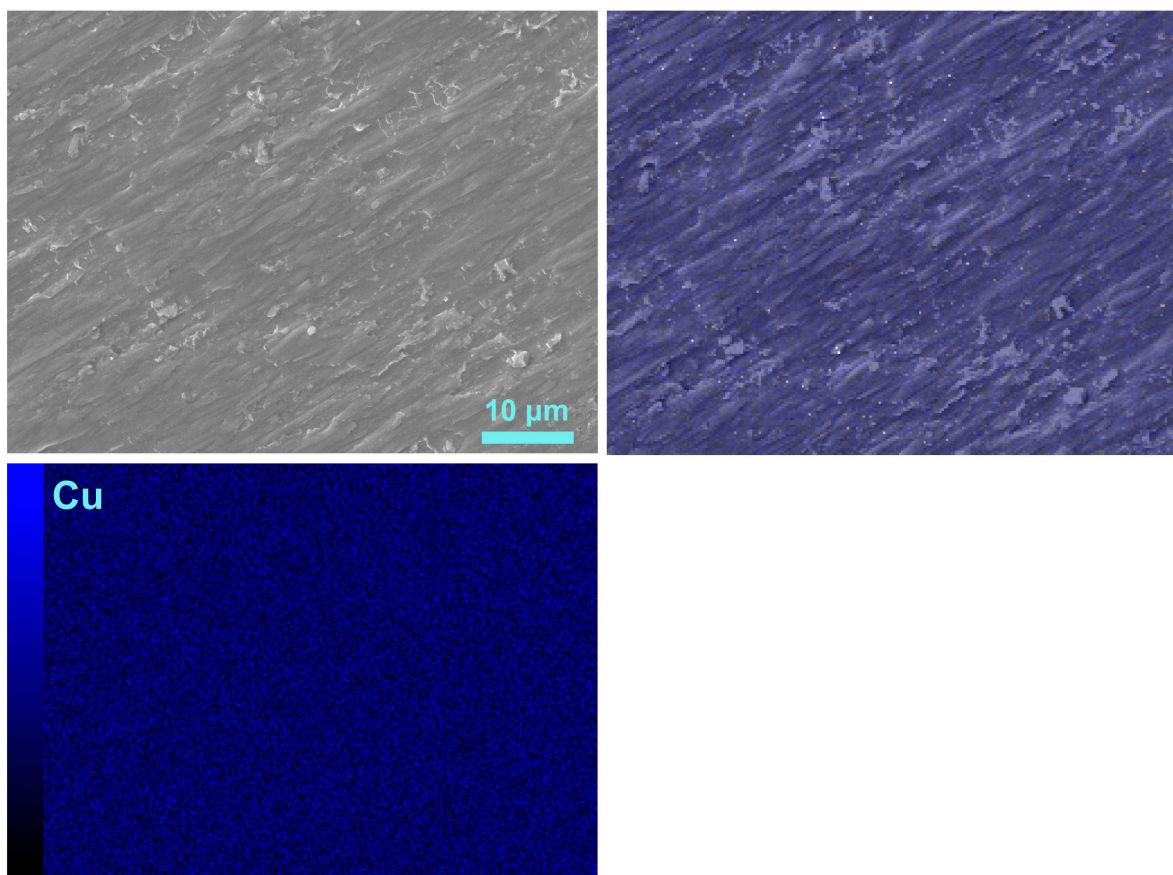


Figure S32. SEM image and EDS analysis of the Cu foil substrate in the fully charged state. As shown, there is no metal particles remaining on the Cu foil substrate, and EDS detects the Cu element only, suggesting a complete Co stripping process.

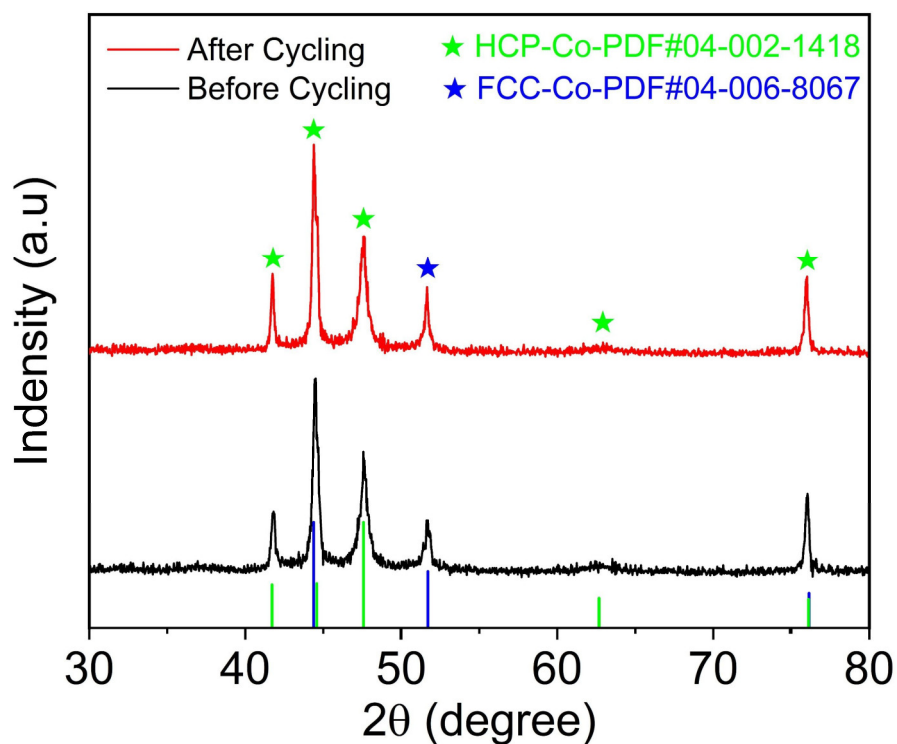


Figure S33. The XRD patterns of the Co self-standing film before and after cycling (100 hours). The condition is 1.0 mA cm^{-2} current for 0.5 mAh cm^{-2} capacity in symmetrical Co|Co batteries. As shown, after 100 hours' cycling, the XRD pattern of the Co electrode is similar to the original electrode, suggesting a reversible plating/stripping process with minimal side reactions.

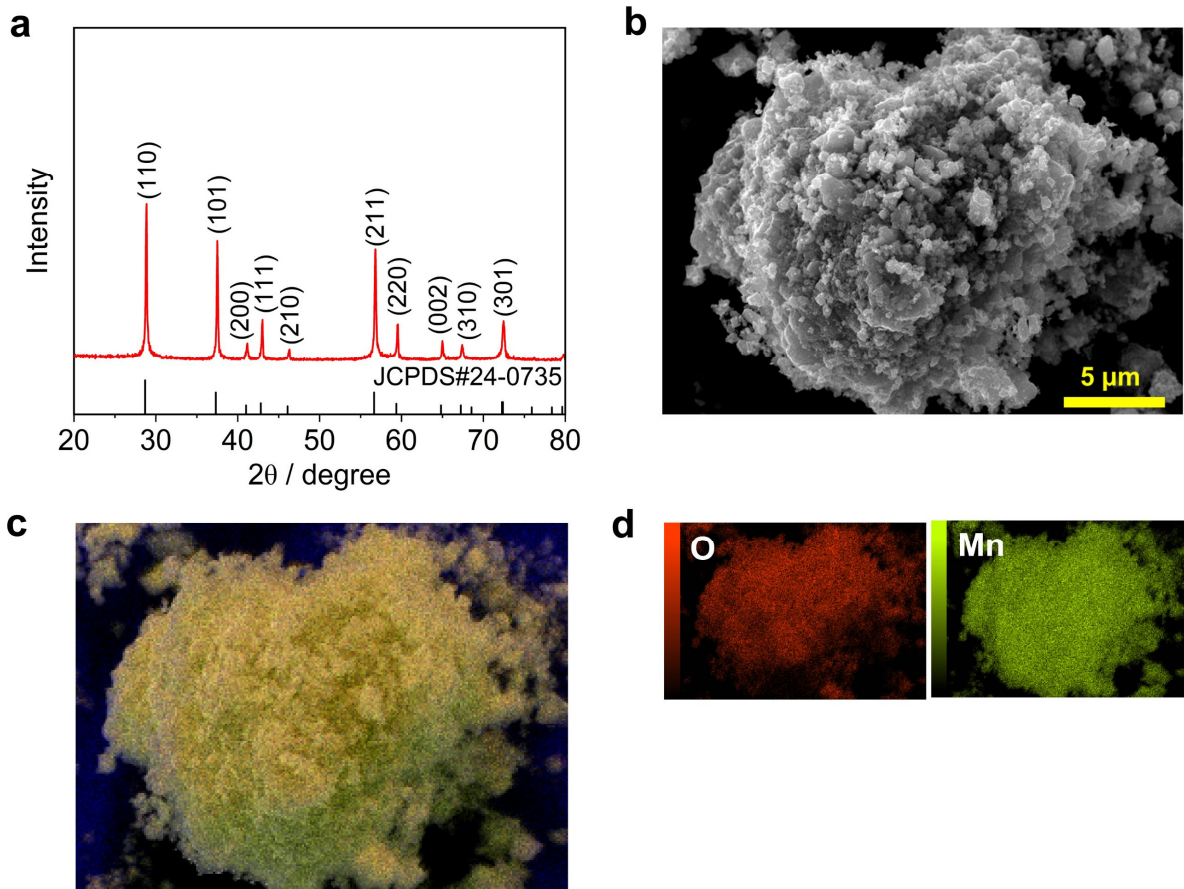


Figure S34. Physical characterizations of the commercial MnO₂ cathode. (a) The XRD pattern; (b) The SEM image; (c-d) EDS mapping results.



Figure S35. The photo of the separator that was retrieved from the Co-MnO₂ battery in 1 M CoCl₂ after cycling.

Table S5. The comparison between the Co-MnO₂ battery with representative metal batteries in terms of capacity, voltage, and energy density.

| Battery system | Cathode capacity / mAh g ⁻¹ | Anode capacity / mAh g ⁻¹ | Average capacity / mAh g ⁻¹ | Cell voltage / V | Energy density / Wh kg ⁻¹ | Citation |
|---------------------|--|--------------------------------------|--|------------------|--------------------------------------|-----------|
| Zn-MnO ₂ | 240 | ~820 | 185.7 | ~1.3 | 241 | [31] |
| Zn-MnO ₂ | 285 | ~820 | 211.5 | ~1.44 | ~304 | [32] |
| Zn-MnO ₂ | 280 | ~820 | 153.5 | ~1.36 | 208 | [33] |
| Zn-MnO ₂ | 385 | ~820 | 262 | 1.3 | 340 | [34] |
| Zn-MnO ₂ | 329 | ~820 | 235 | 1.3 | 305 | [35] |
| Cd-MnO ₂ | 310 | 477 | 188 | ~1.0 | 188 | [11] |
| Sn-MnO ₂ | 255.1 | 451 | 162.9 | 1.5 | 244.3 | [36] |
| In-MnO ₂ | 330 | 700 | 224 | 1.22 | 273 | [37] |
| Co-MnO ₂ | 340 | ~910 | 247.5 | ~0.97 | 240 | This work |

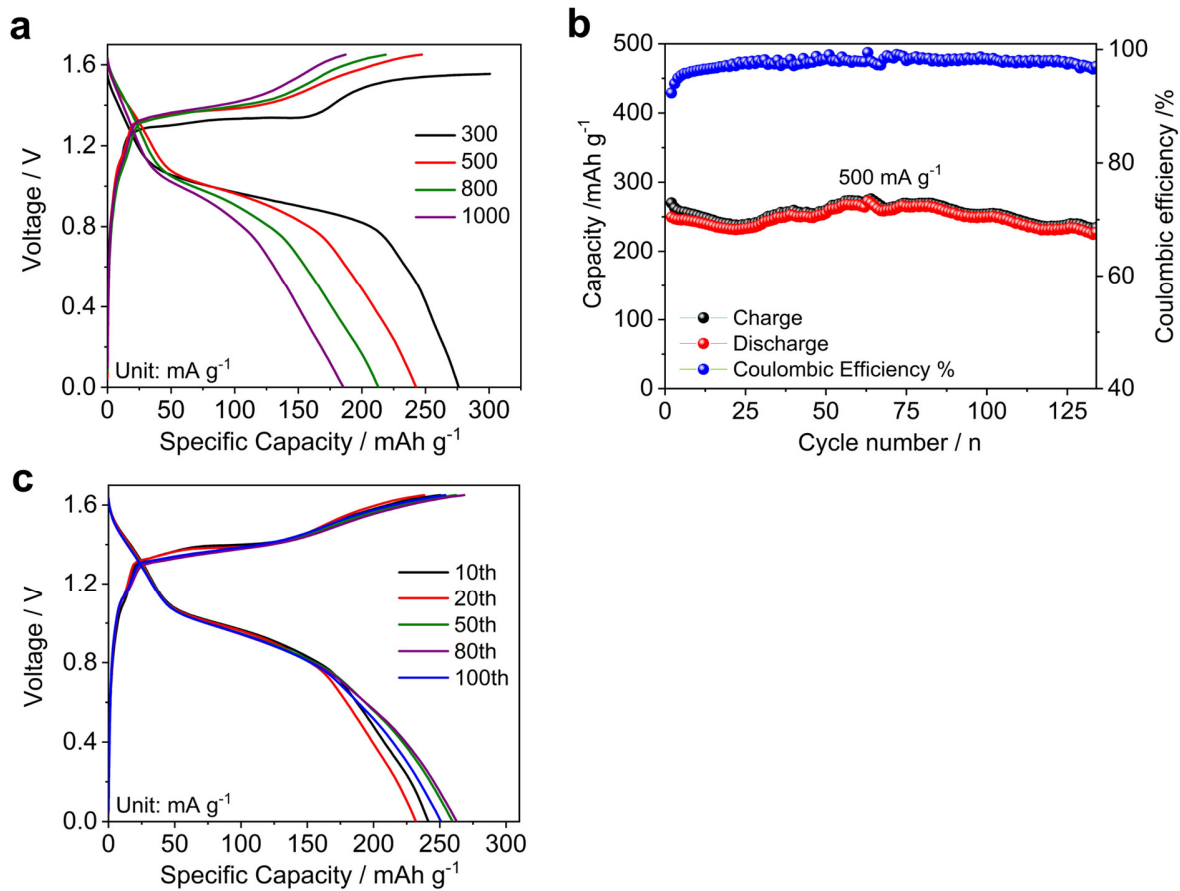


Figure S36. Electrochemical performance of the the Co|MnO₂ battery. (a) Rate performance; (b) The cycling performance; (c) Selected GCD curves during cycling.

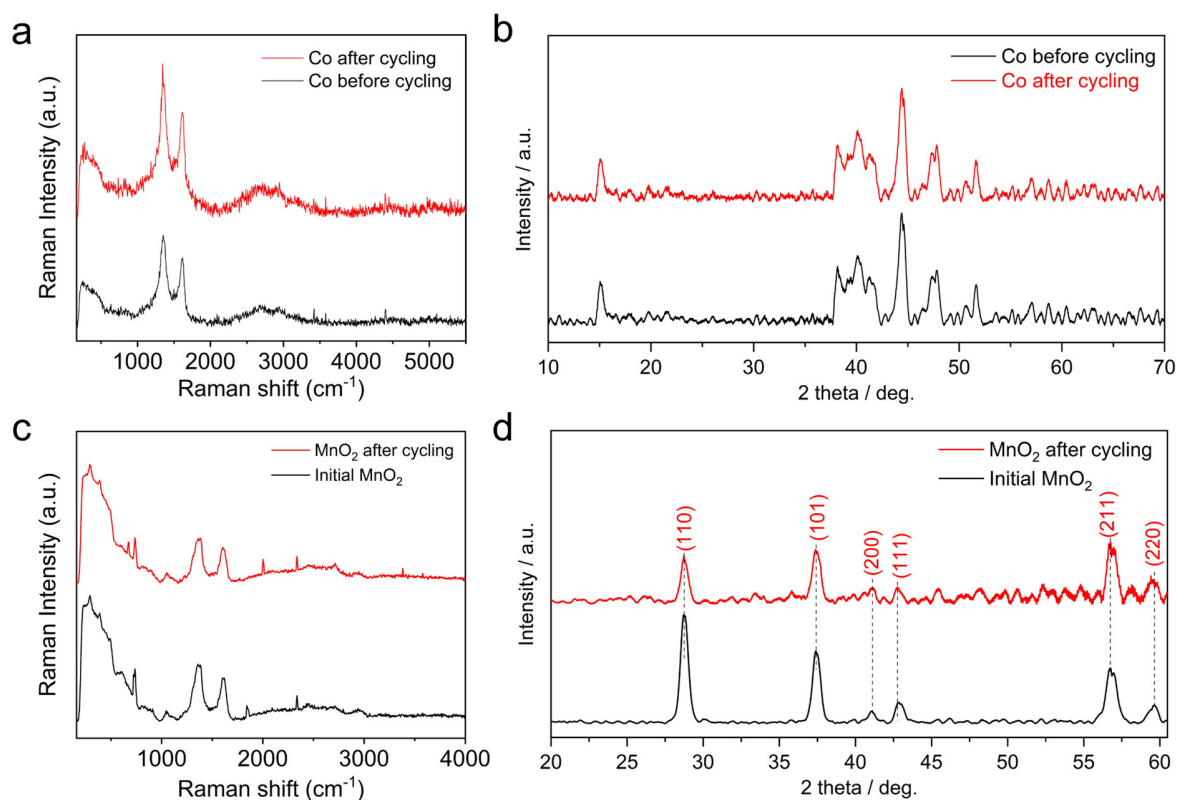


Figure S37. The post-cycling characterization of the Co anode and MnO₂ cathode in the Co-MnO₂ batteries. (a) Raman results of Co electrodes before and after cycling; (b) XRD patterns of Co electrode before and after cycling; (c) Raman results of MnO₂ electrodes before and after cycling; (d) XRD patterns of MnO₂ electrodes before and after cycling.

As shown in **Figure S37a-b**, the cycled Co electrodes demonstrated similar responses in the Raman and XRD tests, suggesting that no Mn-based compounds have been deposited on the Co metal surface. This can be also explained by their redox potential difference: the Co²⁺/Co couple is -0.28 V vs. SHE, which is much higher than the Mn²⁺/Mn couple. Therefore, Co metal cannot reduce Mn²⁺ ions due to thermodynamic limitations. However, the pre-added Mn²⁺ ions could be partially oxidized to MnO_x materials and deposited on the cathode side, due to the relatively high cut-off voltage during charging. *Ex situ* Raman and XRD detected some new peaks for the cycled MnO₂ electrodes (**Figure 37c-d**), implying the possibility of Mn²⁺ ion oxidization and deposition.

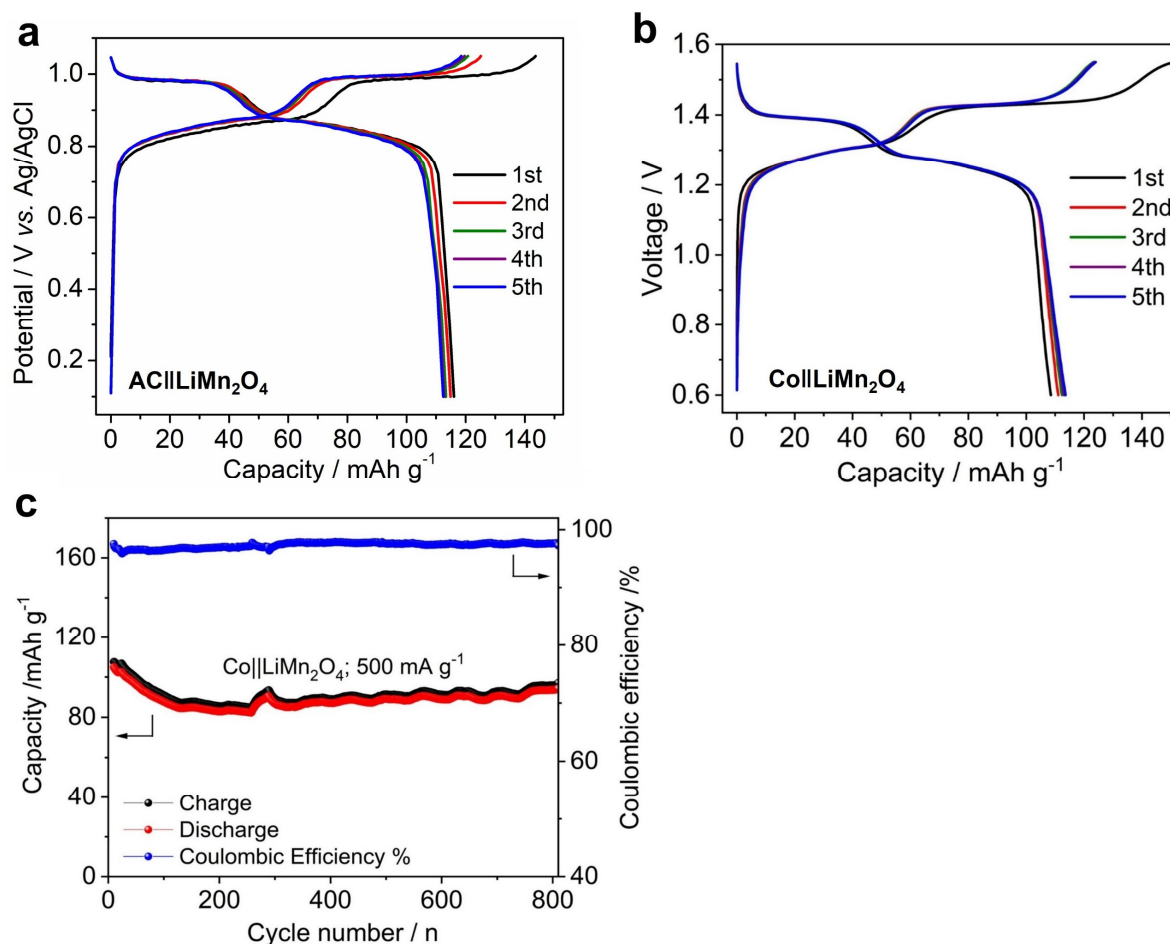


Figure S38. The electrochemical characterization of the LiMn₂O₄ cathode and the Li⁺/Co²⁺ hybrid batteries. (a) GCD curves of the AC||LiMn₂O₄ half cell in the pure 1 M LiCl electrolyte; (b) GCD curves of the Co||LiMn₂O₄ hybrid battery at 100 mA g⁻¹ in the 1 M CoCl₂ + 1 M LiCl electrolyte; (c) The cycling performance of the hybrid battery at 500 mA g⁻¹. AC is short for activated carbon.

It is known that the LiMn₂O₄ cathode preferentially hosts small cations of Li⁺ over other cations. Consequently, the GCD curves of the Co||LiMn₂O₄ hybrid battery (**Figure 38b**) are akin to those in the AC||LiMn₂O₄ battery (**Figure 38a**) with a pure 1 M LiCl electrolyte, suggesting the Li⁺ ion insertion in the LiMn₂O₄ cathode. This hybrid battery exhibits two characteristic discharge plateaus at ~1.4 and ~1.25 V and a good capacity of ~115 mAh g⁻¹. This Li-ion hybrid battery also demonstrates a stable cycling for 800 cycles.

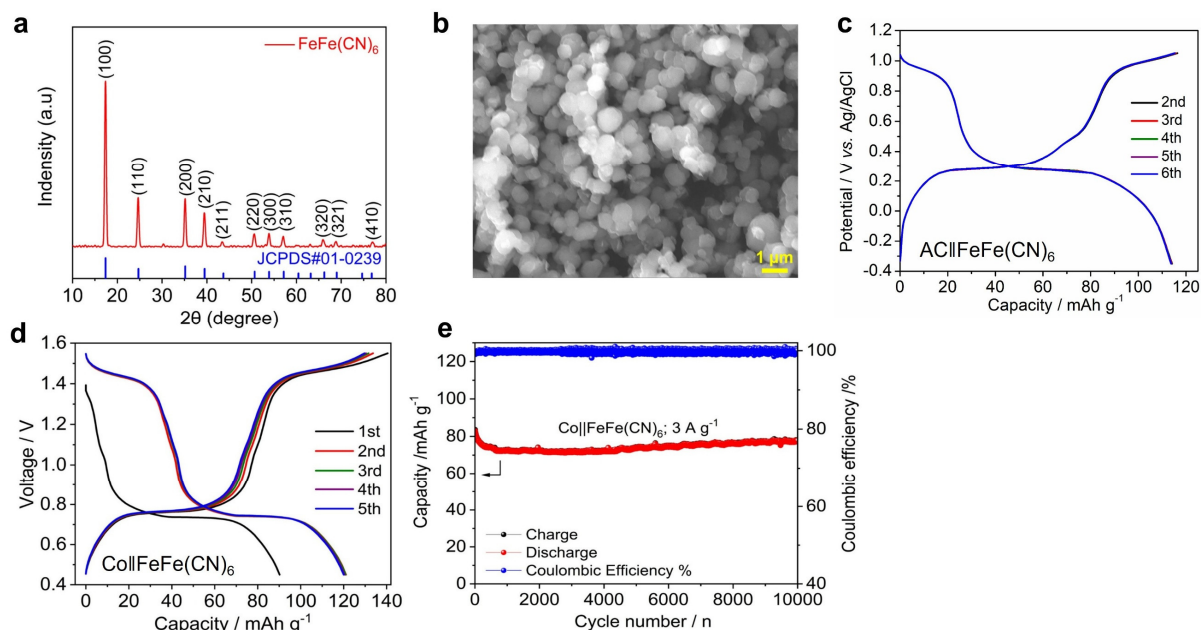


Figure S39. The characterization of the $\text{FeFe}(\text{CN})_6$ cathode and the $\text{K}^+/\text{Co}^{2+}$ hybrid batteries. (a) The XRD pattern; (b) The SEM image; (c) GCD curves the $\text{AC}||\text{FeFe}(\text{CN})_6$ half cell at 100 mA g^{-1} in the pure 1 M KCl electrolyte; (d) GCD curves of the $\text{Co}||\text{FeFe}(\text{CN})_6$ hybrid battery at 100 mA g^{-1} in the $1 \text{ M CoCl}_2 + 1 \text{ M KCl}$ electrolyte; (e) The cycling performance of the hybrid battery at 3 A g^{-1} .

The Berlin green cathode of $\text{FeFe}(\text{CN})_6$ is known for its selectivity toward large cations of K^+ over other cations. Therefore, we assembled a $\text{K}^+/\text{Co}^{2+}$ hybrid battery of $\text{Co}||\text{FeFe}(\text{CN})_6$ in the $1 \text{ M CoCl}_2 + 1 \text{ M KCl}$ electrolyte. This battery exhibits two discharge plateaus of ~ 1.45 and 0.75 V and a discharge capacity of $\sim 121 \text{ mAh g}^{-1}$. The GCD curves of the hybrid $\text{Co}||\text{FeFe}(\text{CN})_6$ battery in $1 \text{ M CoCl}_2 + 1 \text{ M KCl}$ (**Figure 39d**) are akin to those of the $\text{AC}||\text{FeFe}(\text{CN})_6$ battery (**Figure 39c**) in the pure 1 M KCl electrolyte, suggesting the structural selectivity of Berlin green toward K^+ ions. This hybrid battery achieves a very stable cycling life of 10,000 cycles at 3 A g^{-1} .

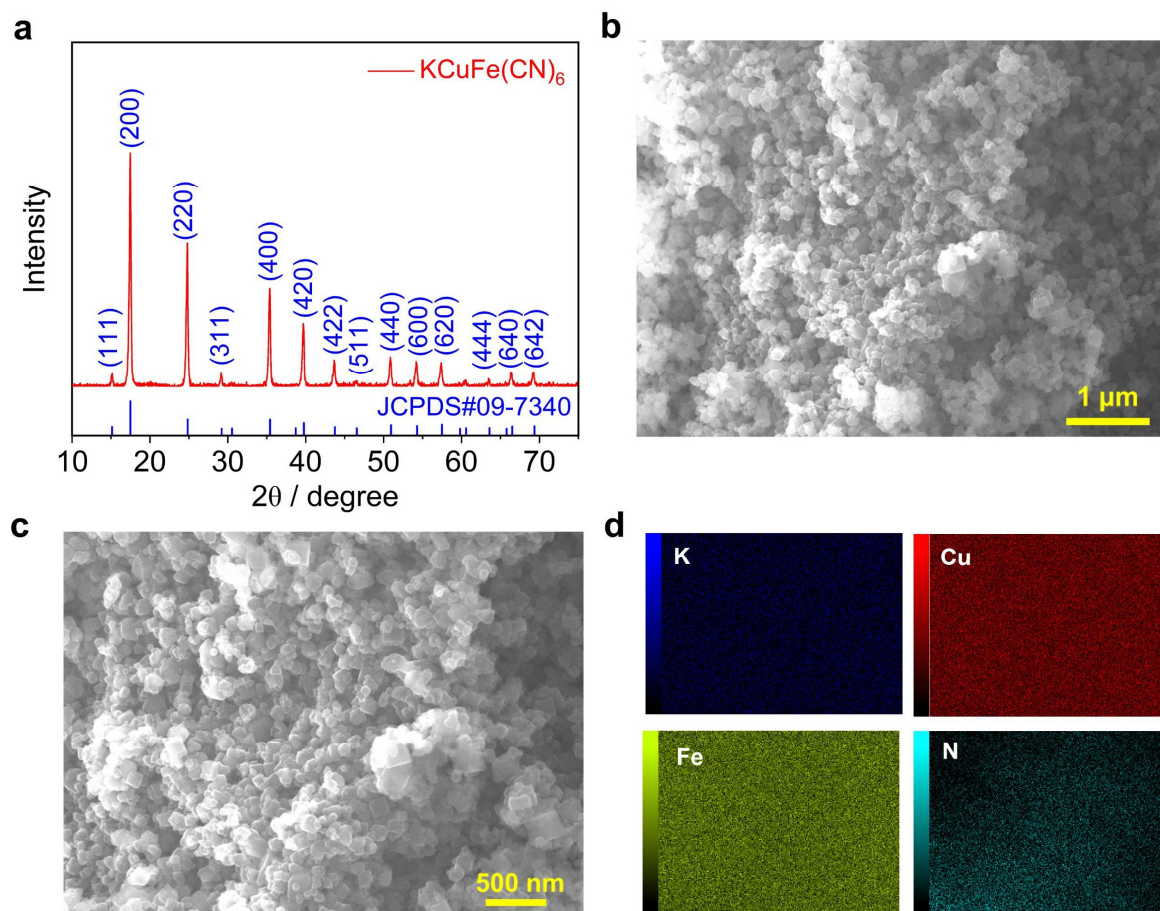


Figure S40. Physical characterizations of the $\text{KCuFe}(\text{CN})_6$ cathode. (a) The XRD pattern; (b-c) The SEM image; (d) EDS mapping results.

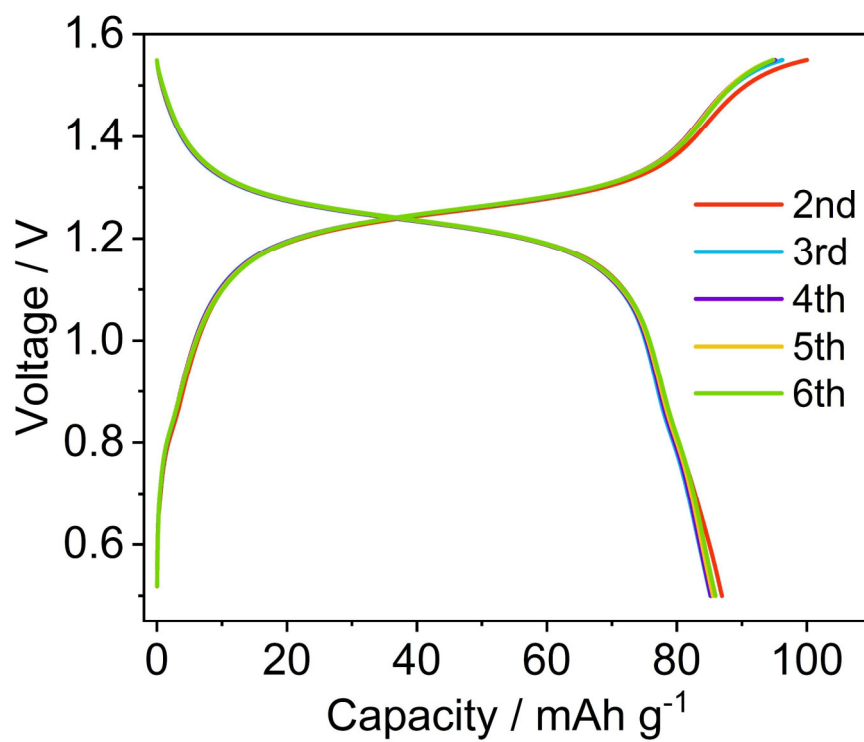


Figure S41. The GCD curves of the hybrid Co||KCuFe(CN)₆ batteries at 100 mA g⁻¹.

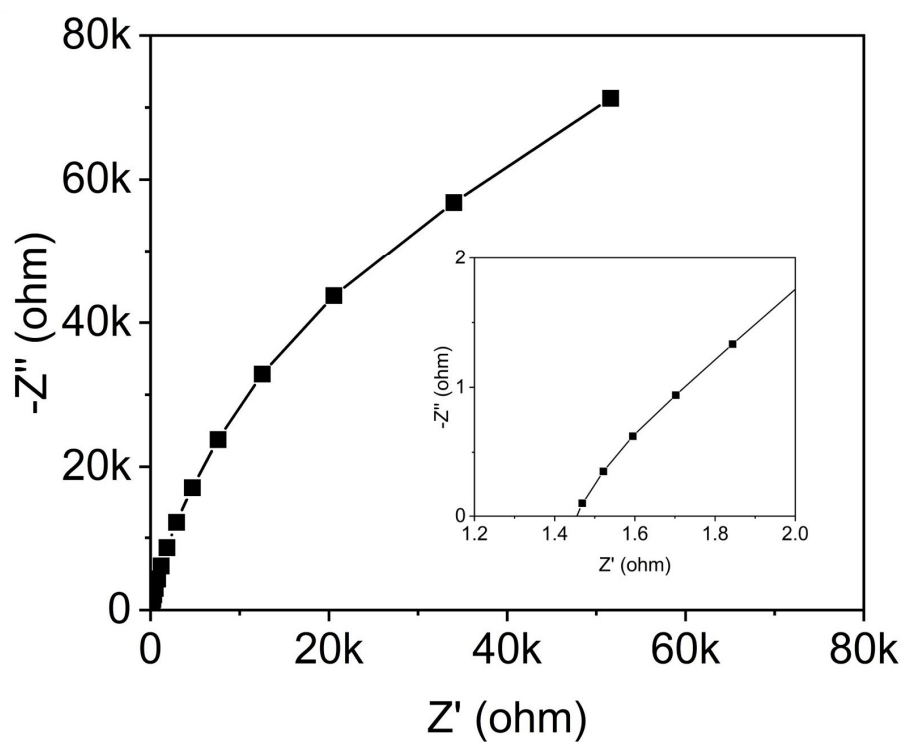


Figure S42. The electrochemical impedance spectra (EIS) result of the 1 M CoCl_2 + 1 M KCl electrolyte, where two titanium rods were used as current collectors.

Based on the solution resistance (1.46Ω), the titanium rod distance (0.14 cm), and the titanium rod area (1.266 cm^2), we can calculate the ion conductivity as 75.74 mS cm^{-1} for the 1 M CoCl_2 solution.

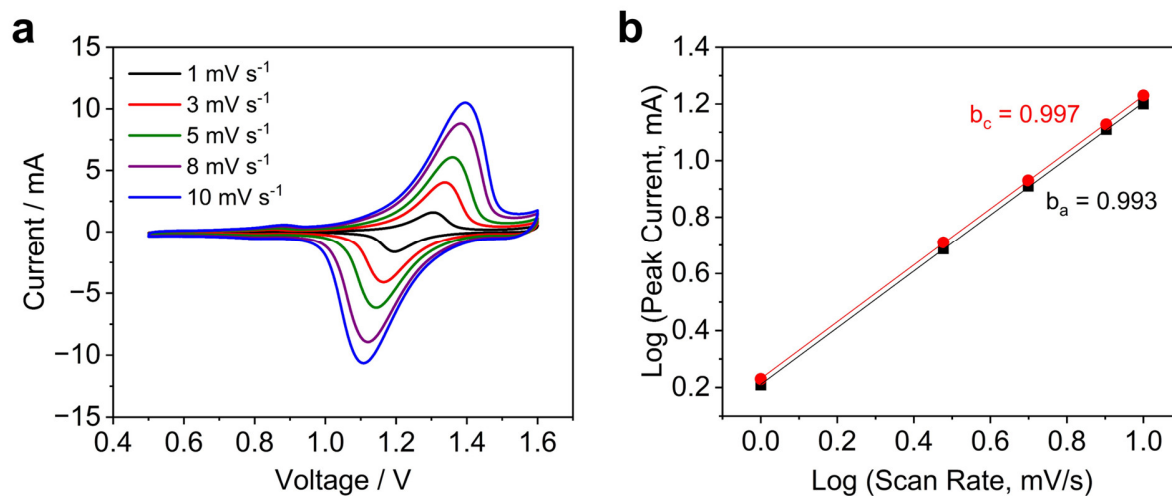


Figure S43. (a) CV curves of Co||KCuFe(CN)₆ batteries at different scanning rates; (b) Relationship between the logarithm of peak current [$\log(i)$] and scan rate [$\log(v)$].

As shown, the b values for the cathodic and anodic peaks are very close to 1, indicating a capacitive K-ion insertion process. This could explain the observed high-rate performance in the hybrid Co||KCuFe(CN)₆ battery.

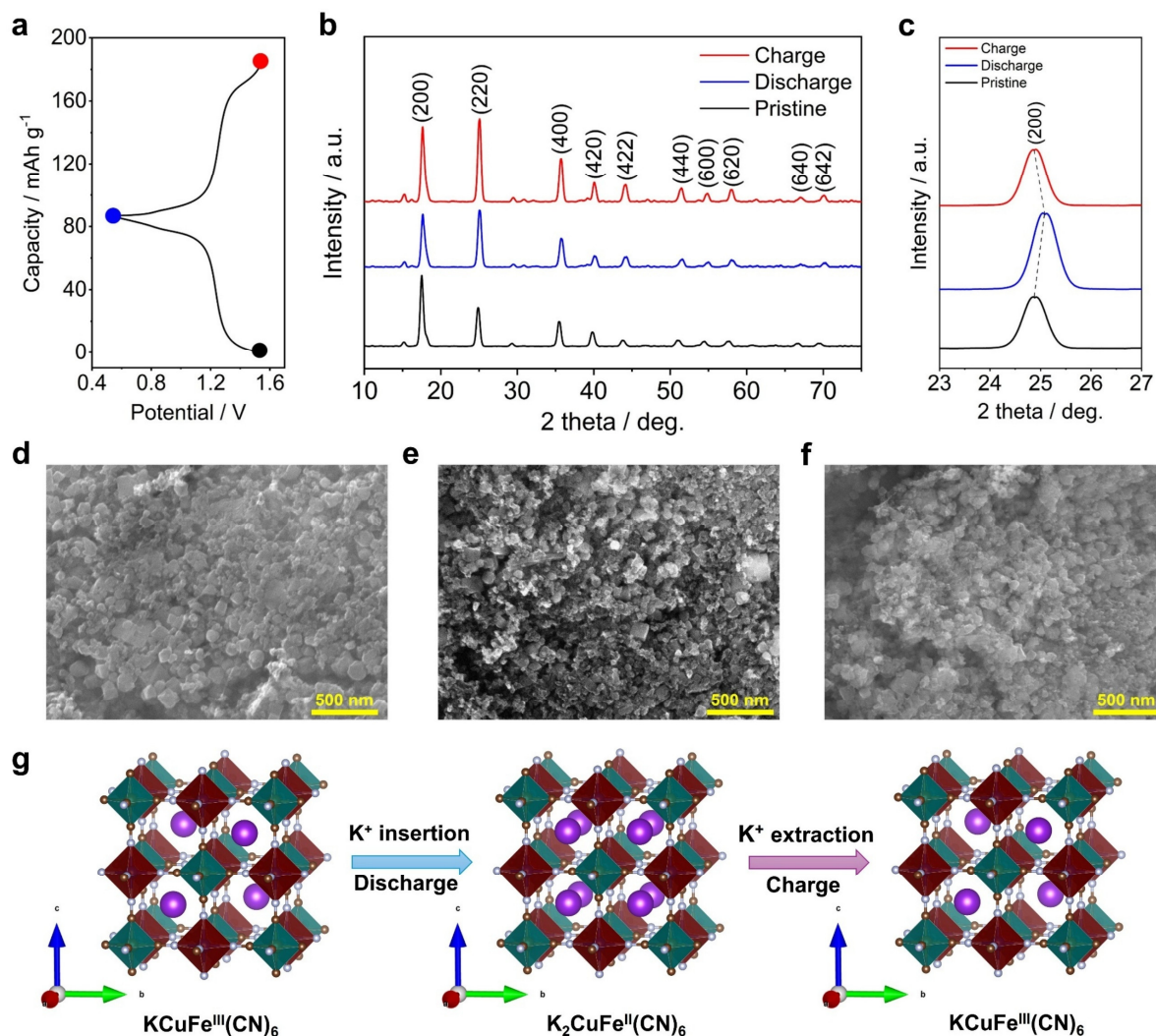


Figure S44. The mechanistic characterization of the $\text{KCuFe}(\text{CN})_6$ electrode. (a) The typical GCD curve; (b-c) The *ex-situ* XRD patterns; (d-f) The *ex-situ* SEM images at different charge/discharge states.

As shown, during the entire discharge/charge process, the $\text{KCuFe}(\text{CN})_6$ cathode maintains similar XRD patterns that are attributed to the typical face-centered cubic phase. This indicates a solid-solution K^+ insertion process, and it agrees well with the S-shaped GCD curves. Careful observation reveals that during the discharge, the (002) peak shifts to a higher position, due to the smaller ionic radius of $[\text{Fe}^{\text{II}}(\text{CN})_6]^{4-}$ than that of $[\text{Fe}^{\text{III}}(\text{CN})_6]^{3-}$. During the charge, the (002) peak restores to its original position, suggesting a reversible structure evolution. Based on the (002)

peak, we can also calculate that the lattice changes from 10.22 Å (charged) to 10.12 Å (discharged), leading to a small volume change of 3%. This minimal structure change well explains excellent cycling stability.

We also utilized SEM to observe the morphological changes. As shown, the KCuFe(CN)_6 cathode demonstrates similar nano-particle morphology with comparable particle size. This is different from the salt precipitation in the MnO_2 case.

Overall, we provide a scheme to illustrate the reversible K^+ insertion mechanism in the KCuFe(CN)_6 cathode.

Reference

1. Harris, *Quant. Chem. Anal.*, Macmillan, 2010.
2. Price of chemical elements; https://en.wikipedia.org/wiki/Prices_of_chemical_elements
3. M. Wang, Y. Meng, Y. Xu, N. Chen, M. Chuai, Y. Yuan, J. Sun, Z. Liu, X. Zheng and Z. Zhang, *Energy Environ. Sci.*, 2023, **16**, 5284-5293.
4. X. Wu, A. Markir, Y. Xu, C. Zhang, D. P. Leonard, W. Shin and X. Ji, *Adv. Funct. Mater.*, 2019, **29**, 1900911.
5. W. Wu, X. Yang, K. Wang, C. Li, X. Zhang, H.-Y. Shi, X.-X. Liu and X. Sun, *Chem. Eng. J.*, 2022, **432**, 134389.
6. J. Liu, D. Dong, A. L. Caro, N. S. Andreas, Z. Li, Y. Qin, D. Bedrov and T. Gao, *ACS Cent. Sci.*, 2022, **8**, 729-740.
7. J. Zhao, X. Yang, S. Li, N. Chen, C. Wang, Y. Zeng and F. Du, *CCS Chem.*, 2021, **3**, 2498-2508.
8. M. Wang, Y. Meng, P. Gao, K. Li, Z. Liu, Z. Zhu, M. Ali, T. Ahmad, N. Chen and Y. Yuan, *Adv. Mater.*, 2023, **35**, 2305368.
9. H. Cai, S. Bi, R. Wang, L. Liu and Z. Niu, *Angew. Chem. Int. Ed.*, 2022, **61**, e202205472.
10. S. Chang, W. Hou, A. Del Valle-Perez, I. Ullah, S. Qiu, J. L. Rodriguez, L. M. Díaz-Vázquez, L. Cunci, G. Morell and X. Wu, *Angew. Chem. Int. Ed.*, e202414346.
11. S. Katiyar, S. Chang, I. Ullah, W. Hou, A. Conde-Delmoral, S. Qiu, G. Morell and X. Wu, *Energy Environ. Sci.*, 2024, DOI: 10.1039/D4EE01615G.
12. S. Chang, L. Lu, I. Ullah, W. Hou, J. F. Florez Gomez, A. Conde-Delmoral, C. M. Font Marin, G. Morell, Z. Chen and X. Wu, *Adv. Funct. Mater.*, 2024, 2407342.
13. L. Cao, D. Li, T. Pollard, T. Deng, B. Zhang, C. Yang, L. Chen, J. Vatamanu, E. Hu and M. J. Hourwitz, *Nat. Nanotechnol.*, 2021, **16**, 902-910.
14. J. L. Yang, T. Xiao, T. Xiao, J. Li, Z. Yu, K. Liu, P. Yang and H. J. Fan, *Adv. Mater.*, 2024, 2313610.
15. S. Chen, S. Li, L. Ma, Y. Ying, Z. Wu, H. Huang and C. Zhi, *Angew. Chem. Int. Ed.*, 2024, **63**, e202319125.
16. X. Shi, J. Xie, J. Wang, S. Xie, Z. Yang and X. Lu, *Nat. Commun.*, 2024, **15**, 302.
17. X. Guo, H. Hong, Q. Li, J. Zhu, Z. Wu, Y. Wang, S. Yang, Z. Huang, Y. Huang and N. Li, *Matter*, 2024, **7**, 4014-4030.

18. S. Chen, S. Li, L. Ma, Y. Ying, Z. Wu, H. Huang and C. Zhi, *Angew. Chem. Int. Ed.*, 2024, **63**, e202319125.
19. H. Jiang, L. Tang, Y. Fu, S. Wang, S. K. Sandstrom, A. M. Scida, G. Li, D. Hoang, J. J. Hong and N.-C. Chiu, *Nat. Sustain.*, 2023, 1-10.
20. F. Wang, O. Borodin, T. Gao, X. Fan, W. Sun, F. Han, A. Faraone, J. A. Dura, K. Xu and C. Wang, *Nat. Mater.*, 2018, **17**, 543-549.
21. C. Y. Chen, K. Matsumoto, K. Kubota, R. Hagiwara and Q. Xu, *Adv. Energy Mater.*, 2019, **9**, 1900196.
22. C. Zhang, W. Shin, L. Zhu, C. Chen, J. C. Neuefeind, Y. Xu, S. I. Allec, C. Liu, Z. Wei and A. Daniyar, *Carbon Energy*, 2021, **3**, 339-348.
23. A. Naveed, H. Yang, Y. Shao, J. Yang, N. Yanna, J. Liu, S. Shi, L. Zhang, A. Ye and B. He, *Adv. Mater.*, 2019, **31**, 1900668.
24. F. Ming, Y. Zhu, G. Huang, A.-H. Emwas, H. Liang, Y. Cui and H. N. Alshareef, *J. Am. Chem. Soc.*, 2022, **144**, 7160-7170.
25. R. Zhao, H. Wang, H. Du, Y. Yang, Z. Gao, L. Qie and Y. Huang, *Nat. Commun.*, 2022, **13**, 3252.
26. L. Geng, J. Meng, X. Wang, C. Han, K. Han, Z. Xiao, M. Huang, P. Xu, L. Zhang and L. Zhou, *Angew. Chem. Int. Ed.*, 2022, **61**, e202206717.
27. D. Han, C. Cui, K. Zhang, Z. Wang, J. Gao, Y. Guo, Z. Zhang, S. Wu, L. Yin and Z. Weng, *Nat. Sustain.*, 2022, **5**, 205-213.
28. B. Zhang and H. J. Fan, *Joule*, 2025, **9**
29. B. Liu, X. Yuan and Y. Li, *ACS Energy Lett.*, 2023, **8**, 3820-3828.
30. C. Zhong, B. Liu, J. Ding, X. Liu, Y. Zhong, Y. Li, C. Sun, X. Han, Y. Deng and N. Zhao, *Nat. Energy*, 2020, **5**, 440-449.
31. W. Sun, F. Wang, S. Hou, C. Yang, X. Fan, Z. Ma, T. Gao, F. Han, R. Hu and M. Zhu, *J. Am. Chem. Soc.*, 2017, **139**, 9775-9778.
32. H. Pan, Y. Shao, P. Yan, Y. Cheng, K. S. Han, Z. Nie, C. Wang, J. Yang, X. Li and P. Bhattacharya, *Nat. Energy*, 2016, **1**, 1-7.
33. J. Huang, Z. Wang, M. Hou, X. Dong, Y. Liu, Y. Wang and Y. Xia, *Nat. Commun.*, 2018, **9**, 2906.

34. Y. Fu, Q. Wei, G. Zhang, X. Wang, J. Zhang, Y. Hu, D. Wang, L. Zuin, T. Zhou and Y. Wu, *Adv. Energy Mater.*, 2018, **8**, 1801445.
35. Q. Zhao, W. Huang, Z. Luo, L. Liu, Y. Lu, Y. Li, L. Li, J. Hu, H. Ma and J. Chen, *Sci. Adv.*, 2018, **4**, eaao1761.
36. H. Zhang, D. Xu, F. Yang, J. Xie, Q. Liu, D.-J. Liu, M. Zhang, X. Lu and Y. S. Meng, *Joule*, 2023, **7**, 971-985.
37. S. Chang, J. F. F. Gomez, S. Katiyar, G. Morell and X. Wu, *J. Am. Chem. Soc.*, 2023, **145**, 24746-24754.